X-ray imaging detector for radiological applications adapted to the context and requirements of low- and middle-income countries

Mario Andrés Chavarria[1*], Matthias Huser[2], Sebastien Blanc[1], Pascal Monnin[3], Jérôme Schmid[4], Christophe Chênes[4], Lazhari Assassi[4], Hubert Blanchard[5], Romain Sahli[5], Jean PhilippeThiran[6], René Salathé[7] and Klaus Schönenberger[1*]

[1)] *EssentialTech Centre, Ecole Polytechnique Fédérale de Lausanne (EPFL), Lausanne CH-1015, Switzerland*

[2)] *Ecole technique - Ecole des métiers - Lausanne (ETML), Lausanne CH-1004, Switzerland*

[3)] *Institute of radiation physics (IRA), Lausanne University Hospital (CHUV) and University of Lausanne (UNIL), Lausanne CH-1007, Switzerland*

[4)] *Geneva School of Health Sciences, HES-SO University of Applied Sciences and Arts Western Switzerland, Genève CH-1206, Switzerland*

[5)] *Pristem S.A. Lausanne CH-1007, Switzerland*

[6)] *Signal Processing Laboratory 5, Ecole Polytechnique Fédérale de Lausanne (EPFL), Lausanne CH-1015, Switzerland*

[7)] *School of Engineering, Ecole Polytechnique Fédérale de Lausanne (EPFL), Lausanne CH-1015, Switzerland*

 (*The authors to whom correspondence may be addressed: klaus.schonenberger@epfl.ch, mario.chavarria@epfl.ch)

(Dated: 31 January 2022)

This paper describes the development of a novel medical X-ray imaging system adapted to the needs and constraints of low- and middle-income countries (LMICs). The developed system is based on an indirect conversion chain: a scintillator plate produces visible light when excited by the X-rays, then a calibrated multi-camera architecture converts the visible light from the scintillator into a set of digital images. The partial images are then unwarped, enhanced and stitched through parallel field programmable gate array (FPGA) processing units and a specialized software. All the detector components were carefully selected focusing on optimizing the system's image quality, robustness, cost-effectiveness and capability to work in harsh tropical environments. With this aim, different customized and commercial components were characterized. The resulting detector can generate high quality medical diagnostic images with detective quantum efficiency (DQE) levels up to 60 % (@ 2.34 µGy), even under harsh environments i.e. 60ºC and 98% humidity.

I. INTRODUCTION

According to the World Health Organization (WHO), more than two thirds of the world's population does not have access to essential X-ray imaging equipment [1]. This "global radiology gap" does not attract as much attention as infectious-disease outbreaks or natural disasters, but it can be as dangerous to the public health and can affect "the entire global health care system" [2]. Too often in low and medium income countries (LMICs), patients die of trivial problems, which could not be treated properly, or were left untreated, due to a lack of access to proper diagnosis. Road accidents, tuberculosis, and complications from childhood pneumonia are recurrent examples of pathologies causing complications that could have been prevented with functional and efficient X-ray imaging services [3]. Even when there are X-ray systems available, a majority are obsolete, based on technologies from 50 years ago or older, such as film-based systems [2,4]. This generates high operating costs and often yields poor image quality [5].

Commonly, when addressing the issue of access to medical technology in LMICs, the main considered factor is the economic, i.e. the purchasing cost. This leads to "well intended" donations of medical equipment which is not adapted to the local context. Such donations are not only useless but they can "actively inhibit healthcare delivery and further burden healthcare providers"[6]. As a result, 'medical equipment graveyards' of obsolete or broken donated biomedical equipment are commonly seen in

hospitals across LMICs [6,7].

To address this problem, the GlobalDiagnostiX project aims to develop, in partnership with local actors in Cameroon, a digital, ultra-robust, and affordable radiological X-ray equipment adapted to the needs and constraints of LMICs. Our methodology [8] relies on three pillars: 1) cooperation and co-creation with local stakeholders in Cameroon (User centered design), 2) interdisciplinarity, with participation of engineers, radiologists, radiographers, anthropologists, designers etc. and 3) entrepreneurship, as the output of the academic work provided the basis for an award-winning start-up company.

A. Field study: Cameroon

Cutting-edge technology is often designed for high-income countries and is expected to work in LMIC. This common and erroneous assumption has led to products that do not work properly nor do they have the intended impact, and, if they do work at first, the implementation and maintenance effort and costs are usually so high that they rapidly fall into disuse [9, 10]. To avoid this issue, the first phase of the project included a field study in Cameroon to define the requirements and expectations of all stakeholders in the pilot country. With this aim, we analyzed the available X-ray medical imaging systems available in the country's healthcare system (FIG 1) and interviewed stakeholders form all the stages of the X-ray technology chain, i.e. physicians, radiographers, medical

equipment distributors, biomedical engineers, academic institutions, NGOs, inspectors and different officials from the ministry of public health of Cameroon (MPHC). The results of this study and videos of some of the interviews are presented in the documentary "X-Ray Machines: Africa's Broken System" [7] and the "Technology Innovation for Sustainable Development" MOOC [11]. Based on the feedback from the stakeholders and the studied literature, the main points to address during the development of the X-ray imaging system are:

FIG 1. X-ray imaging equipment observed in the field study in Cameroon: The equipment in this hospital dates from the 1970's and poses a serious safety risk as the dose of radiation can no longer be measured (©Sylvain Liechti, EPFL2015).

• Digitalization: Over the last decade, digitalization has played a prominent role in the X-ray medical equipment. Film-based and Computed Radiography (CR) plates are being replaced by fully digital X-ray detectors, requiring lower amount of dose and providing better image quality in a very short amount of time. In addition, digital technology enables video capabilities, which has given rise to new applications, such as fluoroscopy, cone beam computed tomography (CBCT) and tomosynthesis. However, due to the mismatch between existing solutions and the local context, modern digital X-ray systems are not widely available in LMICs.

• Cost effectiveness: this should apply to the total cost of ownership, e.g. operation costs, maintenance costs, and not just the purchasing price.

• Robustness: Endemic problems of the local context, such as the lack of quality infrastructure i.e. lack of stable electrical power, which tend to cause frequent and extended downtime, and the scarcity of trained personnel to use and maintain the devices, are an important cause of a reduced lifespan of the X-ray equipment [5]. Additionally, the harsh environment, which involves high levels of humidity and high temperatures, causes high failure rates. The performance and lifespan of digital X-ray equipment, detectors especially, are prone to be compromised at high humidity rate and temperatures [5]. During our field study, we received multiple reports from health personnel in Sub-Saharan countries, that the quality of the X-ray images is degraded when temperature increases above a certain level. Some radiographers even reported that due to this effect, they stopped performing radiographies when temperatures were above "27 or so" degrees Celsius.

• Maintenance and reparability: the lack of replacement parts and the scarcity of trained personnel to do maintenance and repair the devices when they need it highly reduce the utility and lifespan of the few available devices.

B. State of the art

The most common architectures for X-ray digital detectors are flat panels and multi-camera array detectors. Flat panels provide high image quality, i.e. detective quantum efficiency (DQE) values from 40 to 75 %, depending on the configuration and components, which lead to a reduction in the required exposure times and radiation dose rates [12, 13, 14, 15, 16]. However, a major drawback of the flat panel technology is the cost (production, maintenance and replacement) [12]. Flat panel detectors utilize advanced semiconductor components that require costly cleanroom manufacturing processes, which leads to high eventual costs for the final product. Although there are some examples of low costs flat panel solutions in literature, they usually have a lower image quality, i.e. DQE values from 20 to ~35%, or do not provide enough information for a precise comparison [12, 17, 18, 19]. Furthermore, in addition to the purchasing costs, flat panels have high maintenance/repairing costs, e.g. if damaged, the whole detector should be replaced by a specialist at considerable cost. The complexity of the technology also mandates maintenance and repair by specialized personnel, who are not commonly available in LMICs.

The alternative to flat panels, are the multi-camera array detectors, such as the IONA from TeleOptic or the Naomi from RFSystems. These systems generate the images using a scintillator and an array of cameras. Unlike flat panels, the multi-camera detectors do not use large, brittle semiconductor substrates but small image sensors. Therefore, they are more robust and can be produced at a lower cost [20, 21]. However, their lower optical coupling leads to an increase in image noise and a decrease in detective efficiency, i.e. DQE levels from 20 to 40% [22-26].

Commercially available detectors, both flat panels and multi-camera array detectors, usually require ambient temperatures of ~25 °C and maximum operationgon temperatures of 35 °C at relative humidity levels between 30 to 70% [15, 16, 27]. This is a limiting factor for their implementation in many regions in Africa, and other LMICs, where the average temperatures regularly exceed 35 °C, even sometimes reaching temperatures of more than 50 °C, and the relative humidity reaches levels of ≥80 % [28, 29, 30, 31, 32, 33].

C. Proposed solution

The limitations of flat panel technology (e.g. price, fragility, lack of reparability, etc.) sets the multi-camera array based detector a better option for the targeted market. This type of architecture allowed more freedom to design a detector adapted to the needs and constrains of LMICs, such as lower fabrication and maintenance costs, easier maintenance and improved reparability by using "off the shelf" components, which can be easily obtained and replaced on the field, high robustness under harsh environmental conditions, among others.

The developed system implements innovative real-time hardware electronics that comprises multiple Complementary Metal Oxide Semiconductor (CMOS) image sensors. Each image sensor providing a partial image, all captured partial images need to be preprocessed and combined using a specialized software running on an array of parallel processing FPGA units. The image acquisition and processing electronics were designed in easily replaceable modules to reduce complexity of maintenance and repair and to improve the cost efficiency of the solution, i.e. avoiding the need to replace the complete detector if one of its components breaks.

The proposed X-ray detector is based on indirect conversion [FIG 2]: the X-ray photons hit a scintillator screen that emits multiple visible photons upon absorption. These secondary photons form a visible image that is then captured by an array of cameras. Finally, dedicated electronic and computing units such as FPGA chips collect the data from the sensors and send a reconstructed image to an external computer for visualization.
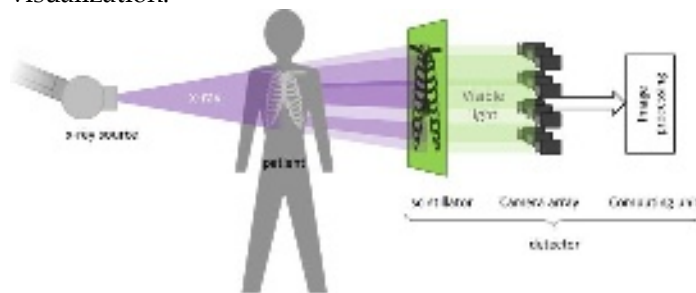

FIG 2. Schematic of the detector's indirect X-ray conversion chain.

The main components of the indirect X-ray conversion chain are:

Scintillator: The scintillator is a key element in the conversion chain. It converts X-rays to visible photons with high efficiency and very low lateral scattering. When an X-ray photon hits an atom of the scintillating material, an electron from the inner orbital is ejected. Surroundings electrons with higher energy will take the empty place by releasing the excess of energy with multiple photons at lower energy (in the range of 2-2.5 eV, visible spectra) [34,35].

Indirect conversion digital X-ray detectors for medical applications often implies one of two types of scintillator materials: Cesium Iodide (CsI:Tl) or Gadolinium Oxysulfide (Gd$_2$O$_2$S:Tb). Both have advantages and disadvantages regarding light throughput, resolution, price, resistance to temperature and humidity, etc.

Lenses: The lens has the role of collecting the visible photons and make them converge to an image sensor, with as little optical aberrations and distortion as possible. Its importance in the conversion chain is not to be neglected: a low quality lens (i.e. aberration, low transmission rate, etc.) leads to bad optical coupling, low modulation transfer function (MTF) and DQE. The specifications of the lens (i.e. focal length, aperture) define the magnification factor (or field of view), which has a direct impact on the minimum distance between the scintillator and the sensor to have a good overlap between the sub-images.

Image sensors: Image sensors are semiconductor chips that embed an array of photodiodes and some integrated electronic to drive and control this array. The designed detector implements off-the-shelf CMOS image sensors to reduce fabrication costs and to ensure easy access to replacement parts. CMOS sensors have several advantages compared to the Thin-Film-Transistor (TFT) technology, commonly used in X-ray flat panel detectors [13, 17, 36]: CMOS sensors can be mass-produced, using standard manufacturing techniques, significantly reducing their costs. CMOS sensors have a low power consumption and offer very fast image acquisition. CMOS technology benefits of silicon substrates offering the best performances and state-of-the-art semiconductor technologies. Additionally, the implemented CMOS sensors are less sensitive to temperature and can operate at higher temperatures than other image sensor technologies [36]. On the other hand, the active area of the CMOS sensor is typically much smaller than the active area from flat panel sensors. Therefore, lenses are used for projection and demagnification of the scintillator image. This reduces the optical coupling leading to a reduction of the final DQE.

During the development phase, each section of the conversion chain was tested using different commercial elements in order to define an optimal set of components to achieve state-of-the-art clinical images under harsh environment conditions. This also provides information about possible replacement parts in case one of the components stop being produced or is not available in the implementation country. Each of the selected components, the development and characterization process and the implemented system architecture are described in detail in the following sections.

II. MATERIALS & METHODS

D. Characterized components

1. *Scintillators*

In order to identify the best X-ray conversion device, in terms of performance and cost, several scintillators (CsI:Tl

and Gd$_2$O$_2$S:Tb) from different manufacturers were analyzed. After a preselection, based on the active area, thickness and resolution, seven models of commercial scintillators were acquired for characterization. TABLE 1 lists the selected scintillators with their main features.

TABLE 1. Characterized commercial scintillators with their main features.

Scintillator	Origin	Technology	Size [mm]	Thickness
SC1(CI)	Japan	Csi:Tl	430x430	400 um
SC2(CI)	China	Csi:Tl	430x430	400 um
SC3(GOS)	Japan	Gd2O2S:Tb	430x430	140 um
SC4(GOS)	Japan	Gd2O2S:Tb	430x430	208 um
SC5(GOS)	China	Gd2O2S:Tb	430x430	390 um
SC6(GOS)	UK	Gd2O2S:Tb	430x430	250 um
SC7(GOS)	UK	Gd2O2S:Tb	430x430	250 um

2. Lenses

Although commercial lenses have a multitude of different mount designs in the machine vision industry, there are three widely used formats, i.e. C-mount, CS-mount and S-mount (also called M12). After a careful analysis of the different lens mountings, the S-mount lenses were selected for the detector design due to their small size, flexibility, low maintenance and cost efficiency. Once the mount type was selected, nine of the most suitable lenses were purchased for characterization (TABLE 2).

TABLE 2. Characterized lenses with their main features.

Lens	Origin	Focal length [mm]	F-stop	Sensor type	Working distance [mm]
L1	Germany	6	1.6	1/2.5	102
L2	Germany	6	1.6	1/2	100
L3	China	6	1.2	1/2.7	97
L4	China	2.8	1.2	1/2.7	55
L5	China	3.6	1.2	1/2.7	68
L6	Germany	6	1.6	1/2	100
L7	Germany	16	1.6	1/2	267
L8	Germany	6	1.2	1/3	105
L9	Germany	8	1.2	1/3	138

Since the lenses present different specifications (e.g., focal length) and design, the field of view is different for each lens. Therefore, the working distance for each lens was set to have a similar image size on the scintillator to that of the reference configuration, i.e. L2 lens @100mm. This allows comparing the lenses efficiency with a fixed camera density for a 43x43cm^2 image size, which is a usual size for a general-purpose medical detector. The determined working distances of all lenses are summarized in the last column of TABLE 2.

TABLE 3. Characterized sensors with their main features.

Image Sensor	Origin	Technology	Color	Resolution	Size
IS1	Japan	Back Illuminated	Monochrome	1936x1096	1/2.8"
IS2	Japan	Back Illuminated	Color	1936x1096	1/2.8"
IS3	USA	Front Illuminated	Monochrome	1280x960	1/3"
IS4	USA	Front Illuminated	Color	1928x1088	1/2.7"

3. Image sensors

The market was screened for cost efficient CMOS image sensors with suitable resolution. Color image sensors use Bayer filters to discriminate photons of a certain wavelength (color). Since the scintillator light is monochromatic (green), only 50% of the sensor pixel will be able to capture the generated image, i.e. the other 50% of the pixels (with red and blue filters) will not be able to capture any light. This significantly reduces the light transmission and therefore the overall sensitivity of the detector. Therefore, the monochrome image sensors represent the best fit for this application. On the other hand, color sensors are more demanded and thus usually more readily available and for a better price. Therefore, a set of 2 monochrome and 2 color sensors were selected, based on the manufacturer specifications, for an extensive comparison according to the EMVA 1288 3.1 standard [37]. The key selection parameters were signal-to-noise ratio (SNR) and sensitivity performance in low light conditions. The selected image sensors, and their main features, are presented in TABLE 3.

The characterization of the IS3 Monochrome and IS4 Color sensors was performed using the evaluation boards provided by the manufacturer. For the IS1 (Monochrome) and IS2 (Color) sensors, commercial cameras were used.

4. Sensor shield

The scintillators do not absorb all the X-ray radiation from the source (the transmission rate varies depending on the type of scintillator and the X-ray spectra). The transmitted X-ray photons interact with all the components behind the scintillator, i.e. the mechanical support, the lenses, the image sensor and the neighboring electronics.

X-ray tests show that the impact of the residual X-ray photons on the image sensor is non-negligible. Part of the residual X-ray photons are absorbed by the image sensor pixels, resulting in very high pixel values in some localized areas (denominated "direct hits") as exemplified in FIG 3. From a medical point of view, the number of direct hits can highly affect the ability to perform a good medical diagnostic, i.e. the white spot artifacts can hide small features, thus valuable information.
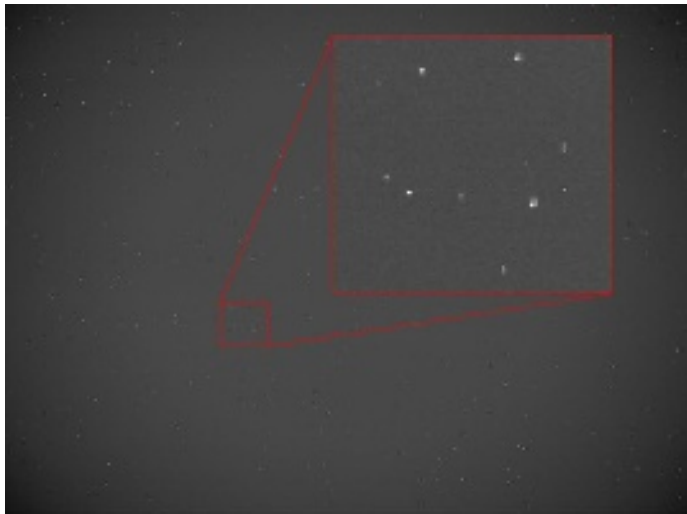
FIG 3. Examples of direct hits (white spots) on a test image taken with no lead glass (@ 80kV 30mAs).

A software solution can be applied to filter out the white spots by detecting and replacing the affected pixels with neighboring pixel values. However, correcting a very high number of direct hits may alter the image and lose too much information for a correct medical diagnosis. Therefore, to avoid losing information, a hardware solution must be added to protect the sensor, in addition to a software-based image correction (Sec IV.C.1).

Lead glass has a high x-ray absorption efficiency and it is transparent to visible light. Therefore, placing a lead glass shield between the scintillator and the camera can absorb the residual X-rays while letting the visible light pass through. X-ray absorbance is linked to the concentration of Pb in the glass, usually given in "Pb equivalent thickness". However, these Pb atoms tends to tint the glass yellow, thus filtering some of the visible light. In order to reach a good trade-off between X-ray absorbance and light transmittance, two types of tests were performed with several Pb equivalent thickness glasses:

- **Hits count:** measurements with shields with Pb equivalent thicknesses from 0 to 3.5 mm and source voltages from 50kV to 200kV were taken. An advanced threshold algorithm was developed to detect and count the number of direct hits in the obtained images (Sec IV.C.1).

- **X-ray absorption:** Light transmittance of shields, with Pb equivalent thicknesses from 0 to 3.5 mm, were measured for the wavelength range of 500nm to 600nm.

E. Image quality assessment

1. X-ray characterization

The assessment of image quality required the measurement of the MTF, the noise power spectrum (NPS) and the DQE [38].

X-ray imaging setup and beam qualities: The detector was characterized for the standard beam quality RQA5 (70 kV – additional filtration of 21 mm Al at the tube exit) defined in the IEC 62220-1 document [39]. A scintillator was positioned 100 mm in front of the sensors and a lead glass of equivalent thickness 1.5 mm lead was interposed behind the scintillator to avoid direct detection by the pixels. The source-to-scintillator distance was set at 132 cm. Pre-processed digital images in a raw 16-bit format were used. The exposure time was varied to give different detector air kerma (DAK). All the images were obtained without an anti-scatter grid. Air kerma measurements were made with a Radcal 9015 dosimeter (Radcal, Monrovia, CA) with a 6 cm³ ionizing chamber. A standard air kerma value of 2.5 µGy was taken as the reference dose level at the detector. Several other target DAK between 0.59 and 18.7 µGy were analyzed.

System response: Uniform images acquired at different DAK were used to measure the relationship between the mean pixel value (PV) and the DAK. Regions of interest (ROI) were selected at the center of each image for calculating the mean pixel value. The system response curve was fitted using a linear function:

$$PV = a + b \cdot DAK , \tag{1}$$

Where a and b are fitted coefficients. The response curve was used to express the image pixel values into DAK levels for the MTF and NPS calculations.

Modulation Transfer Function (MTF): The MTF assesses the spatial resolution of the imaging system. The limit in resolution is often given as the spatial frequency at which the MTF value is equal to 5% [40].

For this study, a tungsten sharp edge was imaged to produce the edge spread function (ESF). The derivative of the ESF gave the line spread function (LSF), the impulse response of the imaging system. The MTF is the magnitude of the Fourier transform of the LSF [41].

Unless otherwise stated, all images for the MTF measurements were acquired using a RQA5 beam with a SC5(GOS) scintillator, L2 lenses and the monochromatic sensor IS1, at a source-to-scintillator distance of 140mm. A lead glass shield of 1.5mm Pb equivalent was inserted between the scintillator and the camera to prevent the residual X-rays from reaching the camera.

Noise Power Spectrum (NPS): The NPS describes the frequency content of the image noise. 2D NPS are the magnitude squared of the Fourier transform of a homogenous ROI on the image that contains only noise:

$$NPS(f_x, f_y) = \frac{1}{A} \langle |\iint_A (d(x,y) - \bar{d}) e^{-i2\pi(xf_x + yf_y)} dx dy|^2 \rangle, \tag{2}$$

Where A is the area of the image, $d(x,y)$ the pixel value at position (x,y), f_x and f_y are spatial frequencies in the x- and y-directions, respectively, and $\bar{d}$ is the mean pixel value in the ROI. The NPS was calculated from three identical homogenous images for each DAK. The normalized noise power spectrum $NNSP(f_x, f_y)$ is the NPS normalized by the square of the mean pixel value:

$$NNPS(f_x, f_y) = \frac{NPS(f_x, f_y)}{\bar{d}^2},\qquad(3)$$

1D NPS curves are radial averages of the 2D NPS, excluding the 0° and 90° axial values.

Detective Quantum Efficiency (DQE): The DQE quantifies the efficiency of the detector to convert incident X-ray photons into digital information. A high DQE value allows using less patient dose for the same image quality. Consequently, optimizing the DQE is a major concern in the design of X-ray detectors. The DQE is the ratio between the output signal-to-noise ratio squared (SNR_{out}^2) and the input signal-to-noise ratio squared (SNR_{in}^2) in the spatial frequency space [39-42]:

$$DQE = \frac{SNR_{out}^2}{SNR_{in}^2},\qquad(4)$$

The DQE is comprised between 0 and 1, 1 being a lossless detector. The DQE is proportional to the square of the MTF, and inversely proportional to the NNPS and X-ray photon fluence (Q).

$$DQE(f_x, f_y) = \frac{MTF(f_x, f_y)^2}{NNPS(f_x, f_y) \cdot Q},\qquad(5)$$

The photon fluence (Q) is given by the product of the DAK and the X-ray fluence per unit DAK (φ):

$$Q = DAK \cdot \varphi \left[\frac{\#photons}{mm^2}\right],\qquad(6)$$

The spectral X-ray fluence per DAK is the number of X-ray photons per surface unit per dose unit [$\#photons/(mm^2 \cdot \mu Gy)$], and depends on the X-ray beam spectrum (kV and filtration) [39].

Spectroscopy: In order to precisely identify the requirements of the imaging sensor, spectroscopy measurements were performed in all the scintillators to determine their emitted light spectrum. Due to the low sensitivity of the spectrometer, high voltage (140kV) and high dose (160mAs) were applied, and no filter was added at the output of the tube during these tests.

2. Visible light characterization

To study the image sensors performance in detail without interferences from external systems (e.g. scintillator, X-ray source, etc.), the image sensors and the developed detection system were tested under visible light: All image sensors were characterized without optics in darkroom conditions. A 525 nm green LED - a wavelength as close as possible to that of the scintillator - was selected as light source. The light source was diffused with an integrating sphere, to achieve the most homogeneous illumination of the sensor. The distance between the sphere output and the sensor plane was set to 100 mm. The

irradiation of the source was measured with a calibrated photodiode and set to 1.0 µW/cm2 (at the sensor plane). Each sensor was set at the smallest gain that achieved the highest pixel reading at saturation, to ensure the full dynamic range is used. A schematic of the implemented measurement setup is shown in FIG 4.

Based on the EMVA1288 standard, different series of images were shot with varying exposure time and constant illumination. Sets of two images were captured with exposure increasing linearly up to pixel saturation with 50 steps, a first series was shot with the light source ON and the second in total darkness. Subsequently, two additional series of 50 images were shot with illumination and exposure times corresponding to 50% of the pixels saturation value. Again, the first series was shot with the light source ON and the second in the dark. Finally, the data from the captured images was processed in order to extract the sensor's intrinsic parameters, e.g. quantum efficiency (QE), gain (K), signal to noise ratio (SNR_{MAX}) and dynamic range.
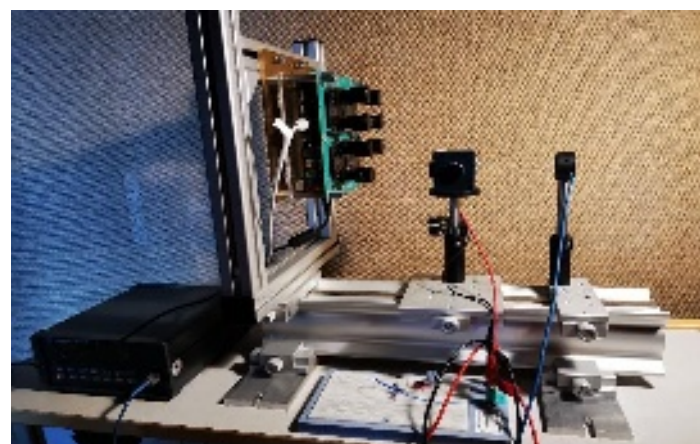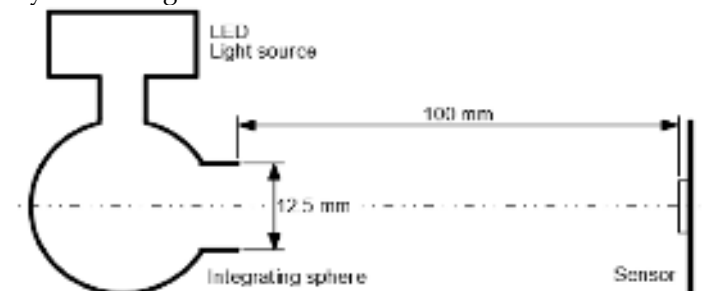

FIG 4. Schematic and picture of the image sensors' characterization setup.

III. COMPONENTS' CHARACTERIZATION RESULTS

A. Scintillators

The selected scintillators were characterized using the methods described in section II.E - "Image quality assessment".

1. MTF

As a result of its intrinsic micro-pillar structure, CsI:Tl scintillators are known to have very good spatial resolution in comparison to other types of scintillator (e.g. Gd_2O_2S:Tb). This is reflected in the excellent behavior

observed with the SC1(CI) scintillator, leading to high MTF values at low and high spatial frequencies with the best measured cut-off frequency (4.52 lp/mm). The other CsI:Tl scintillator, the SC2(CI), shows relatively low MTF values at low spatial frequencies but recovers after 2 lp/mm, reaching a cut-off frequency of 4.07 lp/mm.
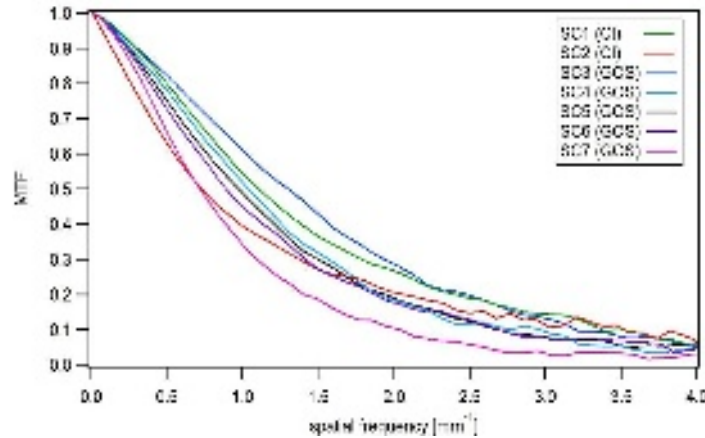

FIG 5. MTF curves of all tested scintillators under RQA5, 1.5mm Pb equivalent lead glass.

The Gd$_2$O$_2$S:Tb scintillators were expected to show lower MTF levels than the CsI:Tl scintillators due to their powder structure. Surprisingly, the SC3(GOS) obtained the highest MTF at low spatial frequencies. However, its MTF rapidly decreases above 2 lp/mm, which leads to a cut-off frequency of 3.99 lp/mm. The SC5(GOS) showed an average behavior at low and medium spatial frequencies. Nevertheless, its MTF remains almost flat at high frequency leading to the second highest high cut-off frequency from the measured scintillators, i.e. 4.28 lp/mm. The SC7(GOS) has very poor MTF levels, probably due to its higher thickness compared to the other Gd$_2$O$_2$S:Tb scintillators. It only reached a 2.6 lp/mm cut-off frequency, below the minimum 2.8 lp/mm required for film-screen X-ray detectors intended to radiological applications.

2. DQE
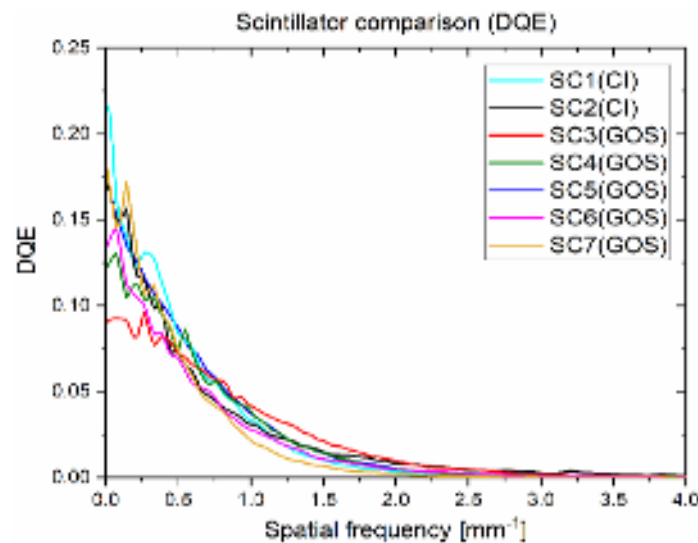
FIG 6. DQE curve comparison of the tested scintillators @18uGy.

Due to its high thickness and absorption rate, the SC1(CI) Scintillator has the highest low-frequency DQE. The SC2(CI) shows relatively poor performance for a CsI:Tl scintillator. Surprisingly, the SC5(GOS), a low cost Gd2O2S:Tb scintillator, produced the third highest DQE levels amongst the measured scintillators. The SC7(GOS) outperforms the SC2(CI) and the SC5(GOS) with a DQE(0) of 18.4%. The high DQE(0) levels of the SC5(GOS) and the SC7(GOS) can be explained by their thicker active layer, i.e. higher absorption. However, higher thickness can lead to poorer MTF, due to more lateral diffusion in the scintillating layer. This is especially critical in the case of the SC6(GOS) and SC7(GOS).

3. NNPS vs. temperature
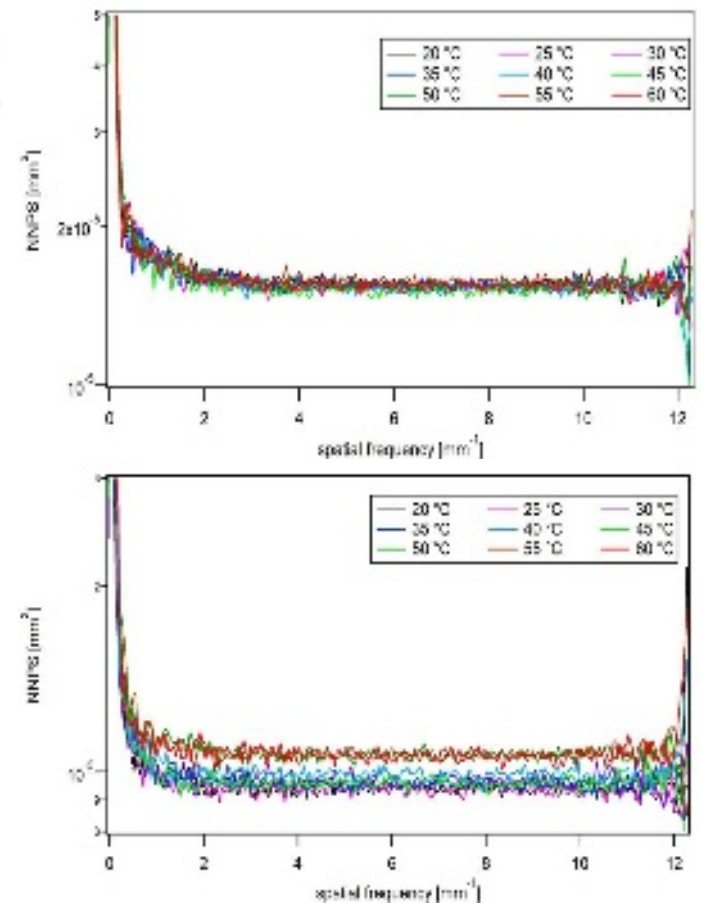
FIG 7. NNPS curves for the SC3(GOS) (top) and the SC2(CI) (bottom) at different temperatures.

The X-ray detector will operate in harsh environments, where ambient temperature can reach up to 45°C with 100% relative humidity. The Gd2O2S:Tb scintillators are known to be very robust and stable, however, the CsI:Tl can suffer of image quality loss at high temperatures and humidity [43]. The impact of the temperature on image noise (NNPS) was measured for two scintillators at different temperatures, i.e. the SC3(GOS) (Gd2O2S:Tb) and the SC2(CI) (CsI:Tl). The resulting NNPS curves are shown in FIG 7.

As expected, the SC3(GOS) exhibits no change over the

tested temperature range. Conversely, the SC2(CI) exhibits an increase of the NNPS by about 10% at high temperature (>45ºC). Since the NNPS is inversely proportional to the DQE, this would lead to a 10% decrease in DQE when used at a temperature over 45°C.

4. Spectroscopy

The CsI:Tl scintillators have a very broad emission bandwidth (from approximately 470nm to 640nm), thus the peak value is lower compared to Gd2O2S:Tb. All Gd2O2S:Tb scintillators exhibit a high peak emission at around 545nm and few other peaks at around 490nm, 580nm and 620nm (FIG 8).
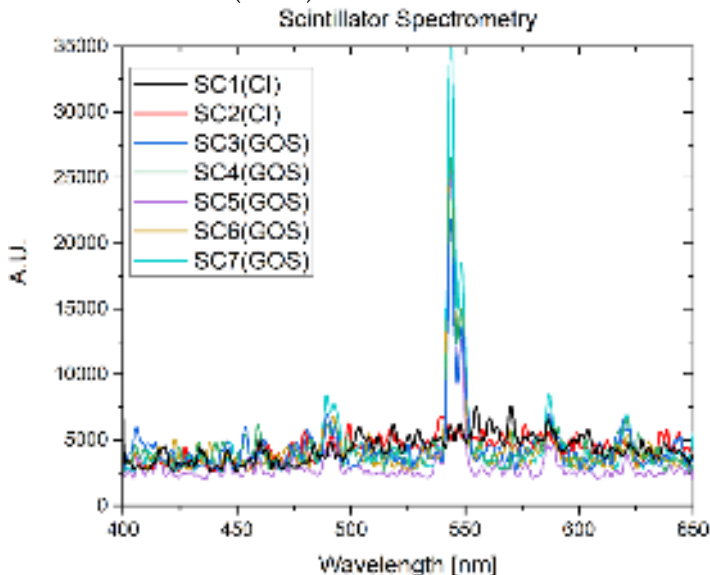
FIG 8. Emitted light spectra of the tested scintillators.

5. Performance and cost analysis

The SC1(CI) showed the best image quality amongst the tested scintillators. However, it has some drawbacks inherent to CsI:Tl scintillators, e.g. higher price, performance decrease at high temperature and degradation due to humidity [44] (CsI is slightly hygroscopic, i.e. tends to absorb moisture from the air [45]). This can be problematic for their implementation in an X-ray detector intended for low-income tropical countries. The other CsI:Tl scintillator, the SC2(CI), exhibited the same drawbacks as the SC1(CI) with a lower image quality.

SC6(GOS) and SC7(GOS) scintillators are cost-effective but showed very poor performances with the exception of a very good DQE(0) for the SC7(GOS). However, this is at the expense of the MTF, which leads to a cutoff frequency below the minimum required for film-screen X-ray detectors intended to medical applications. The SC3(GOS) and SC4(GOS) scintillators (both from the same manufacturer) were the most expensive amongst the tested Gd_2O_2S:Tb scintillators, however their performance, both in MTF and DQE, was below average.

The SC5(GOS) outperformed all Gd_2O_2S:Tb scintillators in MTF and DQE (except for the SC7(GOS) at low

frequency (DQE(0)). Also, it does not suffer from image quality loss due to high temperature and humidity (Gd_2O_2S:Tb is not hygroscopic [46]). Moreover, it is the most cost efficient of all tested scintillators. This makes it a promising candidate for an X-ray detector intended for low-income tropical countries.

B. Lenses

1. MTF

The measured MTF for the different lenses are presented in FIG 9. The MTF were measured at the center of the image, where the focus of the lens is optimal. Due to Seidel's curvature of field effect, edges of an image tend to be slightly out-of-focus when the center is in focus. This effect depends on the lens characteristics, size of the object and image, and the focal distance. To determine the effect of the out-of-focus aberration, the MTF at the edge of the images was calculated and compared to the center values. As expected, the MTF measured in the edge is lower than the MTF in the center, however, the maximal variations are low (<0.03).
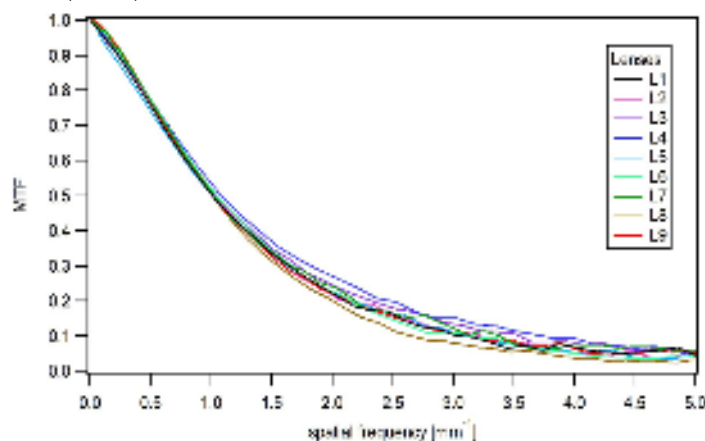

FIG 9. MTF comparison of all lenses, with the SC5(GOS) scintillator and IS1 sensor, RQA5 beam (70kV and 20mAs).

All the characterized lenses show a similar MTF behavior. The 1270XX12MP-M12 lenses slightly outperform the others in terms of spatial resolution, which is surprising given their low price. On the other hand, the German L8 lens has the lowest spatial resolution. Nevertheless, its cut-off frequency (3.75 lp/mm) is still much higher than the minimum required.

2. DQE

DQE(0) vs. focal length: The higher the focal length, the lower the DQE. This is explained by the fact that with lower focal length, the camera is closer to the scintillator (for imaging the same area), thus more photons reach the image sensor. Nevertheless, low focal length usually comes with more geometrical aberration for such small size, low cost lenses, i.e. little room for aberration correction. Therefore, a trade-off between light collection and image distortion must be carefully defined.

DQE(0) vs. F-stop: The F-stop is linked to the numerical

aperture and the lens entrance pupil. The wider the entrance pupil (or the lower F-stop), the more light can pass through the lens. Therefore, the lower the F-stop, the higher the DQE. However, a higher quality lens with higher F-stop can have a higher DQE(0) than a lower quality lens with lower F-stop. Such is the case of the L6 (f 1.6) which has a higher DQE(0) than two of the lenses (L3 and L5) with lower F-stop (1.2). This shows that, despite the theoretical features described in the datasheet, the lens performances are highly dependent on the quality of manufacturing.
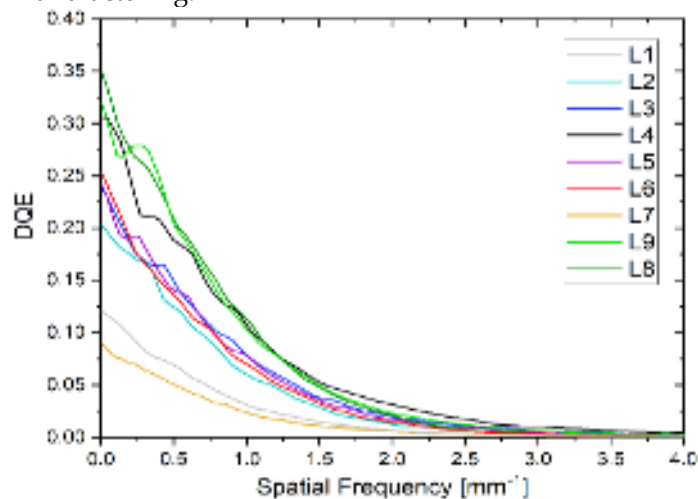
FIG 10. DQE comparison of all lenses, with the SC5(GOS) scintillator and the IS1 sensor, RQA5 beam (70kV and 3.10mAs, 2.5uGy)

3. Performance and cost analysis

After analyzing the experimental results, lenses with focal length 6 mm represent the best tradeoff between geometric distortion, field of view, and light throughput. In addition, 6 mm focal length lenses are very common in the market. Therefore, they are easy to obtain, there are many models to choose from and their prices are low in comparison to more specialized optics.

The L8 lens is the best candidate for the detector system. It gave the best zero-frequency DQE levels from the measured lenses at an acceptable cost. Its main drawback is its low MTF, which however remains higher than the minimum required.

C. Image sensors

The measured sensitivity and SNR plots for all characterized sensors are presented in FIG 11. For the color sensors, only the green channel was considered (50% of the pixels). Therefore, to account for the loss of sensitivity due to the Bayer filter, the pixel surface was considered be that of two pixels. TABLE 4 summarizes all the characterized sensors and measured metrics.
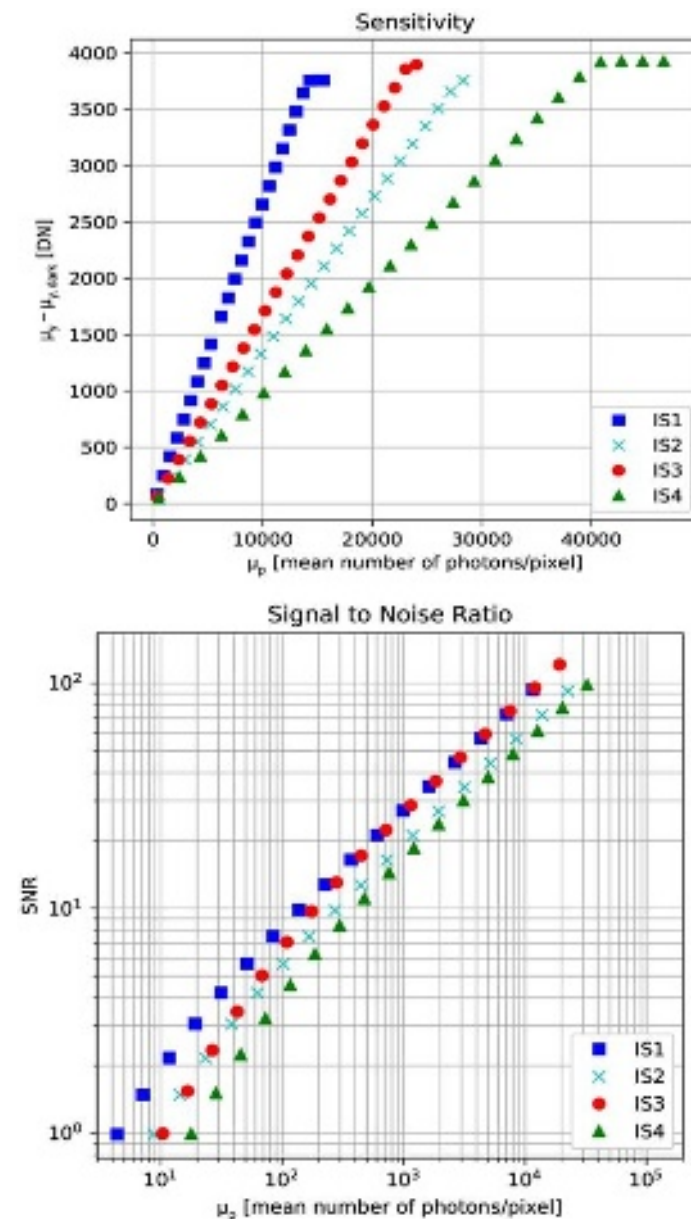
FIG 11. Image sensors characterization results for sensitivity and signal to noise ratio (SNR). μ_y is mean value of light image in digital value (DN) and $\mu_{y\ dark}$ the mean value of dark image in DN to remove in order to make black equal to 0 (removal of pedestal level).

TABLE 4. Main data results from the sensors' characterization.

Parameter	Unit	IS1	IS2	IS3	IS4
Pixel size	μm	2.90	2 x 2.90	3.75	2 x 3.00
Quantum efficiency	%	75.1	37.8	76.0	29.9
System gain	DN/e$^-$	0.36	0.36	0.22	0.33
Temporal dark noise	e$^-$	2.67	2.71	7.30	4.74
Absolute sensitivity threshold	p	4.38	8.81	10.4	17.8

1. Sensitivity

The sensor's sensitivity is given by its mean pixel response to light (in digital number (DN)). The fixed irradiation, wavelength and exposure time were used to compute the number of photons per pixels for each measured point. All sensors showed linear responses up to saturation. The IS1 (FIG 11 (top) - dark blue squares) shows the best sensitivity behavior from the measured sensors. This can be explained by the "back-side illuminated" technology used in its design. In "back-side illuminated" sensors, the photodiode is located over the integrated circuit and metal lines (opposite to traditional C-MOS sensors), this reduces the light scattering and reflection, thus more photons reach the photodiode (improving the sensitivity and reducing the noise). The IS2 sensor uses the same technology as the IS1, however, its results are below the monochrome version. This is due to the fact that only 50% of its pixels are able to detect green light (Bayer filter), therefore, half of the photons are lost.

2. SNR

The signal-to-noise ratio (SNR) is computed by dividing the mean value of an image with homogeneous illumination by its standard deviation. EMVA 1288 standard proposes a camera model with a single internal noise source that is the sum of dark and quantization noise. The number of photons also fluctuate statistically (shot noise), this phenomenon is not negligible for a small number of photons.

Results in low light conditions, with a low number of photons, are of most interest for the X-ray detection application. Since it would be difficult to properly measure the SNR with an illumination of only some photons, the EMVA 1288 standard proposes a computation to extrapolate the SNR based on the fitted camera model. The plotted curves correspond to this extrapolation and make the absolute sensitivity threshold visible i.e. absolute sensitivity threshold corresponds to the point where the noise is equal to the signal and thus the smallest amount of photons detectable by the camera. Again, the IS1 Monochrome (**FIG 11** (bottom) – dark blue squares) shows the best behavior from the characterized sensors, especially in low light condition, thanks to its low-noise technology.

3. Performance analysis

Multiple CMOS sensors were tested according to the EMVA1288 standard. Low light performance is the key factor in selecting the correct sensor for this application. Results showed that the new IS1 outperforms all other tested sensors in that regard. Therefore, it is a good candidate for the multi-camera array X-ray detector.

D. Sensor shielding (Lead glass)

In order to reach a good trade-off between X-ray absorbance and light transmittance, different tests were performed, at 20 mAs and 30 mAs, with several Pb equivalent thickness glasses (from 0.5 to 3 mm). Since the lead glass absorption rate depends on the energy of the X-ray photons, three series of tests were performed at 70, 80 and 120kV. The detection and counting of the direct hits were done with a customized threshold algorithm (Sec. IV.C.1).

Placing the lead glass shield in front of the sensor resulted in a dramatic reduction of the number of direct hits: the higher the Pb equivalent thickness the lower the number of direct hits, i.e. higher X-ray absorption rate, until 1.5 mm where it stabilizes in an average hits reduction of around 93%. The remaining hits can be attributed to the diffusing and back-scattering X-ray photons due to the setup.

The drawback of using a lead glass shield is a reduction in the light transmittance. Transmittance measurements, for a wavelength range from 500nm to 600nm, showed a light absorption of around 7% by the 0.5mm Pb equivalent thickness, which increases to 14 to 16% for the ≥1.5mm Pb equivalent thicknesses. This absorption will have a direct impact on the DQE, since the cameras will collect less light. However, this loss is considered acceptable in comparison to the benefit of having X-ray shielding to prevent residual X-ray photons to hit the sensor.

These results showed that, with a hit reduction of more than 93% and a reduction in light transmittance of less than 14%, the 1.5 mm Pb equivalent thickness glass is the best option to protect the sensors and other system electronic components from residual X-ray hits.

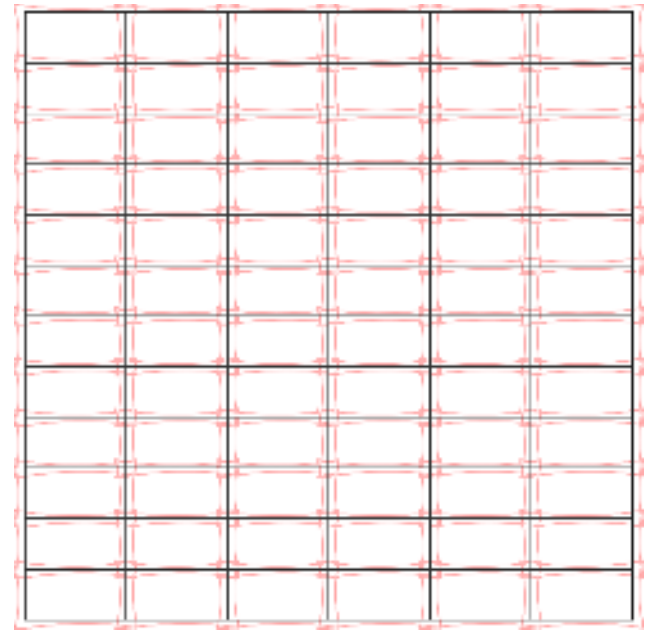## IV. IMAGE DETECTOR: DESIGN & ARCHITECTURE

FIG 12. Sub-image distribution for a 6 by 12 cameras .

The detector architecture consists of multiple multi-camera modules (4 camera per module), that comprise the CMOS image sensors, a computational unit (an FPGA) and memory (SRAM) to buffer the data. A master unit will

collect the pre-processed images coming from these multi-camera modules and finalize the stitching. Based on the characterization results presented in the previous sections, the components showing the best compromise in terms of price, environment resistance and performances were selected (optimum configuration): the German lens L8, the monochromatic IS1 sensor and a lead glass of 1.5mm Pb equivalent thickness. With this configuration, and based on the tests results, an optimal scintillator to image sensor distance of 98.72 mm was determined. Taking into account the geometric distortion correction and the minimum overlap, this results in a matrix of 6 by 12 cameras (72 in total), as depicted in FIG 12.

A. Image sensors

In an electronic imaging module embedding the selected image sensor was developed (FIG 13 , FIG 14 and FIG 15). The 4xIS1 module embed four IS1 CMOS image sensors and their respective lens holders. Each 4-camera module uses 1 Intel FPGA Cyclone IV EP4CE22F17 chip to buffer the image in a small 32MB dedicated SRAM memory. Special care was taken to design low noise power supplies and lengths and impedance matched data paths to enhance signal integrity and minimize contribution of the board electronic noise to the sensors. The FPGA includes some pre-processing algorithm to correct the flat image (for structured noise correction) and dark image (for electronic noise correction), by applying the bad pixel correction (Sec. IV.C.1) and by averaging series of flat and dark images to reduce the noise impact. The implemented topology enables to configure gains and exposures of many modules through a single master unit, as well as triggering a simultaneous image capture from all sensors. The modules are designed to be mounted on a backplane circuit through a high-speed connector system. This structure enables a region of the detector to be easily replaced for maintenance, if need be. Finally, the images are gathered by the FPGA master to be held at disposition of the control computer. Distributing the computing power to multiple modules makes the electronic architecture more complex. However, it also reduces the workload of the master unit and simplifies its interface.
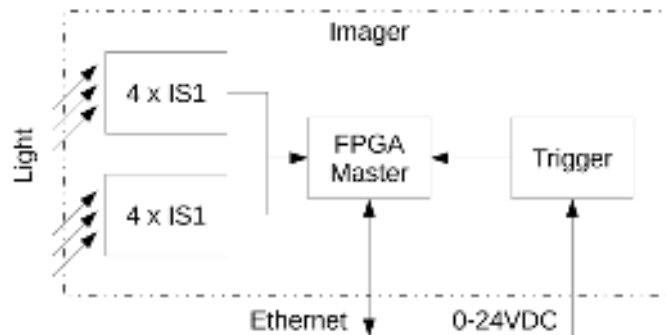
FIG 13. Bloc diagram of two imaging modules and the master unit with external connectivity
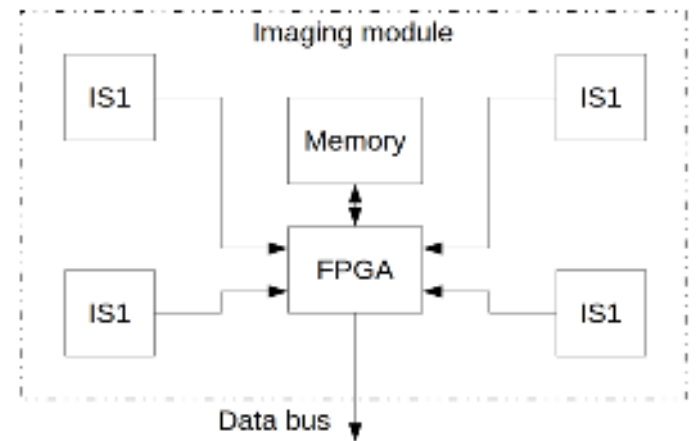
FIG 14. Bloc diagram of the architecture of the imaging module with sensors, memory, FPGA and processor
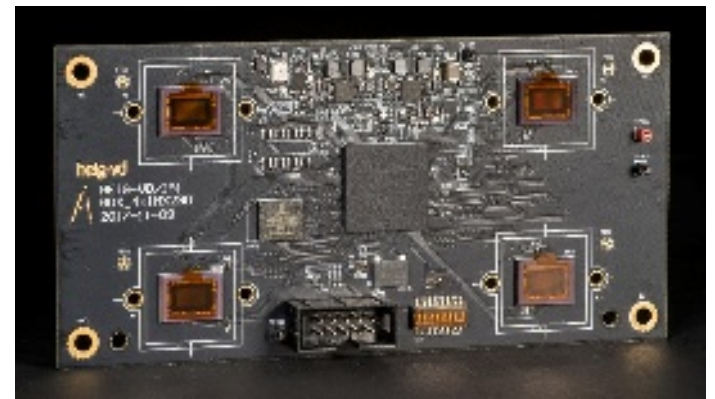
FIG 15. Module 4xIS1 (6 layers PCB with controlled impedance, BGA components)

B. Master unit

A demoboard Terasic DE1-SoC was selected as master unit. The main task of the master unit is to interface all multi-camera modules by configuring the image sensors through SPI bus. The master unit also triggers all the cameras at the very same time in order to avoid any desynchronization between the sub-images. Once the pre-processed data from the multi-camera unit is retrieved into the master unit, it will finalize the image reconstruction in order to output a reconstructed image to an external PC via Ethernet protocol.

C. Image processing

Each image sensor will produce a *raw image* corresponding to an imaged area of the scintillator, which is affected by a variety of intensity and geometric artifacts. Stitching is the operation that consists in assembling raw images into a final pre-processed image, which should not present any of these artifacts nor any observable assembly cues. Strictly speaking, basic (e.g., histogram equalization or edge enhancement) and advanced [47] image post-processing operations are not part of the stitching process and so they are beyond the scope of this paper. The overall stitching process is depicted in FIG 16 .
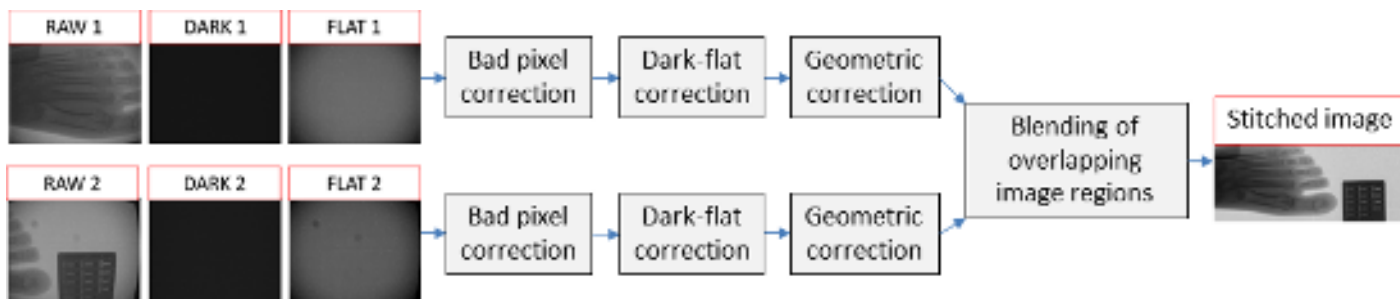
FIG 16. Overview of the stitching pipeline exemplified with a two cameras setup.

1. Bad pixels detection and removal

Bad pixels refer to pixels with abnormal intensity such as dead (always off) or hot (always on) pixels. Such stuck pixels appear progressively over time due to sensor degradation and their position can be detected and permanently recorded. Hot pixels are also the result of X-ray direct hits not corrected by the sensor shielding solutions. By detecting the bad pixels, we can replace their intensity by a weighted average of their neighboring pixel intensities. Our bad pixel detection is based on the analysis of excessive deviations of pixels intensity in the raw and flat images compared to smoothed versions obtained by median filtering. For instance, the hot pixel detection uses at first a maximum filter that detects in small 3x3 image neighborhoods the local maxima. Then a hot pixel is chosen among these maxima if the difference of its intensity between the original and the smoothed images is larger than a threshold.

2. Dark-flat intensity correction

Bad Based on dark and flat images, raw images are corrected to get rid of the intensity inhomogeneity caused by the vignetting effect – mainly characterized by a light falloff far from the image center. Dark images are acquired in total darkness without X-ray emission while flat images are radiographs acquired without anything in front of the scintillator. The dark-flat correction is simple: $I = k(I_r - I_d)/(I_f - I_d)$, where I_r, I_f and I_d are the raw, flat and dark images. Parameter k is a normalizing factor usually computed as the average of all pixel intensities of $(I_f - I_d)$. When correcting images from multiple sensors, the constant k must be identical for all sensors to avoid global intensity inhomogeneity between corrected images I.

3. Geometric correction

Each camera sensor S_i is modeled as a pinhole camera characterized by the estimated intrinsic and extrinsic parameters [48]. Intrinsic parameters include the intrinsic matrix K_i related to the lens characteristics (e.g. focal distance, pixel size) as well as tangential and radial distortion parameters r_i modeling the non-linear deformation of the lens. Extrinsic parameters express the rigid transform $T_i = (R_i, t_i)$ from a world coordinate system CS_w to a camera coordinate system CS_i, where R_i and t_i are the rotation and translation of the rigid transform.
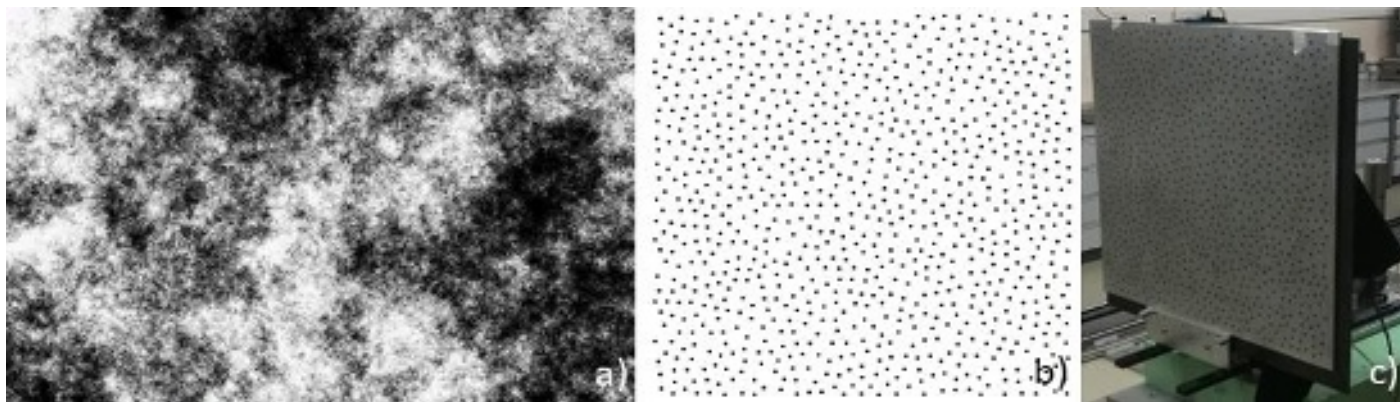
FIG 17. Camera calibration patterns: **a)** point cloud pattern used for intrinsic calibration and **b)** random dots pattern [50] used to manufacture **c)** the extrinsic calibration aluminum plate.

Intrinsic calibration can be performed for each camera independently and with visible light using a calibration pattern. We selected a point cloud pattern (FIG 17a) from OpenCV library [49] that allows partial visibility of the pattern – a very useful feature given the small field of view and short focal distance of the camera sensors. In case of extrinsic calibration, we need to ensure that all cameras share the *same* world coordinate system CS_w in order to estimate the spatial positioning and orientation of each camera with respect to each other. This is achieved by using a calibration pattern simultaneously imaged by all cameras and whose parts can be unambiguously detected. The acquisition must be done with *X-ray emission* as the conversion from X-rays to visible light takes place on the

plane of the scintillator. Hence, the calibration pattern must not only offer partial detection but should be also X-ray "compatible" as well as easy to manufacture. In this context, we chose the random dots pattern from Oyamada et al. [50] composed of dots (FIG 17b) that can be easily drilled on an aluminum plate (FIG 17c), yielding highly contrasted features in the radiographs.

Based on the estimated calibration parameters, a geometric correction process is applied on each sensor image I_i: (1) image undistortion produces rectified images without lens distortion using intrinsic parameters K_i and r_i; (2) homography transformation converts the rectified image in the common world CS and resamples it to match a desired image resolution. The homography is computed from K_i and extrinsic parameters R_i and t_i. The geometric correction can be seen as an *unwarping* process using deformation maps, which can be preprocessed and applied very efficiently in hardware (e.g. FPGA).

4. Blending

Unwarped images will present some overlapping regions as depicted in FIG 18 a. A successful dark-flat correction coupled with a gain compensation approach [51] will produce consistent image intensities across overlapping regions. This consistency avoids the need to identify frontiers in overlapping regions used to avoid so-called *seam* blending artifacts [52]. Similarly, advanced blending (e.g., multiband blending [53]) is not necessary and we can apply a simple weighted linear blending (also known as feathering) where weights are computed from distance maps of the unwarped image regions. As a result, the blending is simple, deterministic and very efficiently executed – yielding excellent stitching results as depicted in FIG 18 c. Further examples of X-ray images taken with the developed system and processed with the described approach are presented in FIG 19.
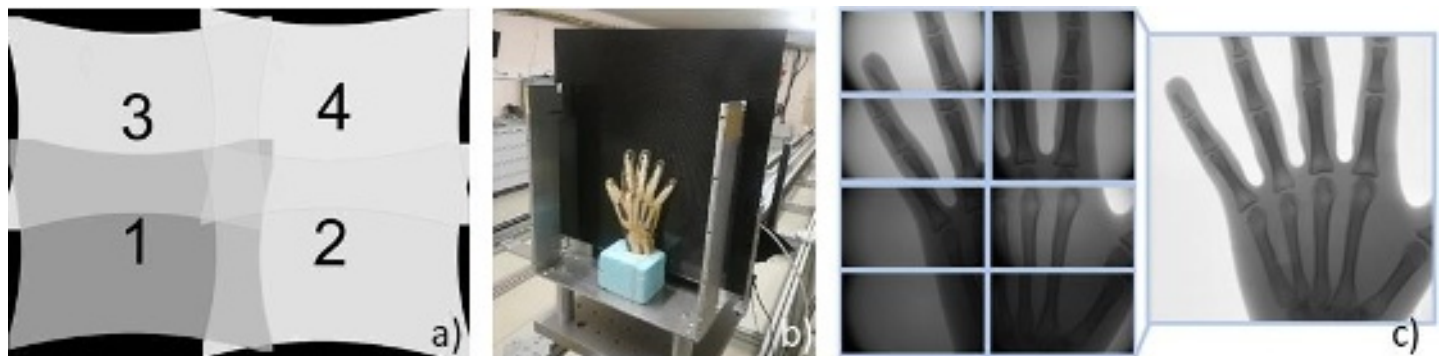
FIG 18. Blending and stitching: a) after geometric correction images will present overlapping areas that will be seamlessly blended into a final stitched image. An example of stitched image of a hand phantom (b) and the produced X-ray image with eight of the detector image sensors is shown in (c).
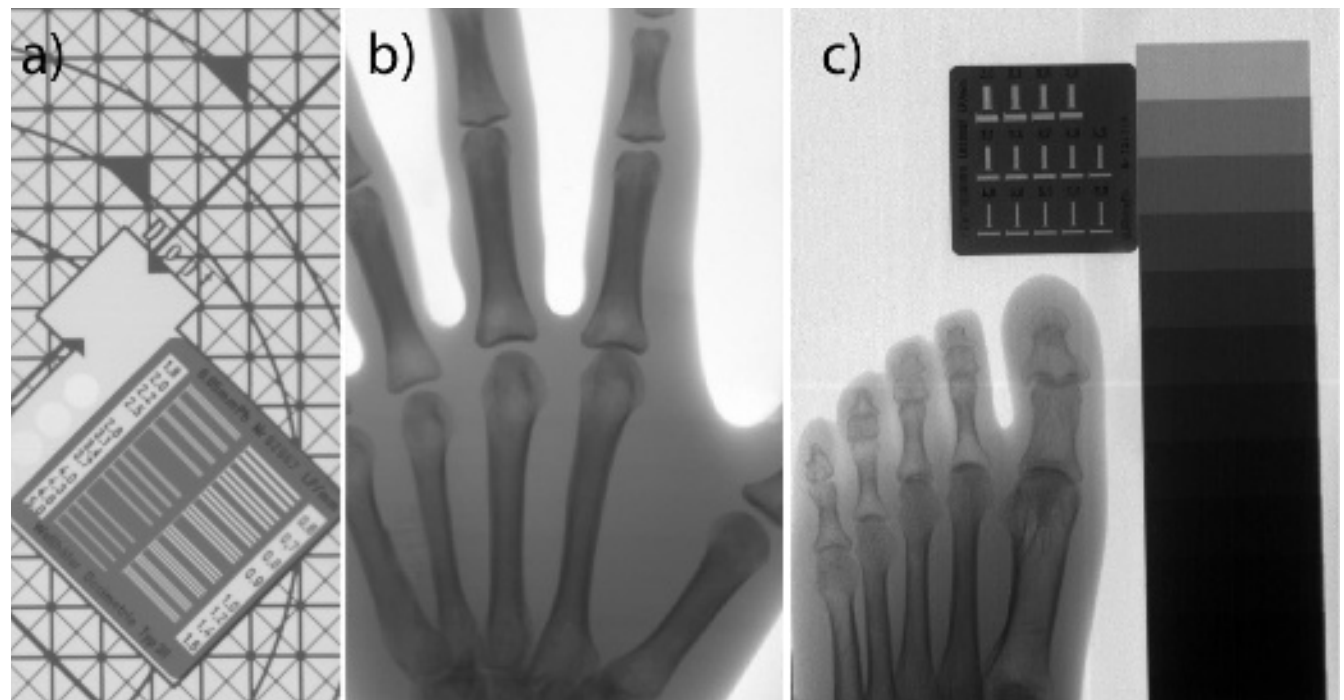
FIG 19. Examples of X-ray images taken with the developed prototype and processing approach: (a) ETR calibration device (70 kV,

50 mAs), (b) zoomed in detail of the hand image in FIG 18 (44 kV, 50 mAs) and (c) foot image with calibration patterns (48 kV, 40 mAs). The central vertical and horizontal bright lines in the right image are not artefacts of the stitching approach but they represent the projection of metallic wires used to hold together the imaged objects.

V. RESULTS

A. Multi-camera module performance

Two types of multi-camera modules were assembled (GDX_IS1_LR and GDX_IS1_SR) implementing linear and switching voltage regulators, respectively. Switching Voltage regulators have a higher power efficiency compared to linear regulators but they can add undesired electronic noise to the system. Both modules were tested with visible light and with X-rays.

B. Visible light characterization

The visible light characterization of the developed multi-camera module was performed with the same method as the image sensor characterization (Section characterization (Section II.E.2), using the setup described in FIG 4. The first module to be characterized was the GDX_IS1_SR. In the initial measurements, a line pattern was visible on the image in low light conditions. This pattern was always present but randomly positioned. The pattern is presumably caused by the "line-by-line" method that the integrated analog-to-digital converter uses to read the sensor pixels. Because of the line-wise nature of the process, a small variation of the converter reference voltage could induce a faint line pattern, which is negligible in daylight conditions but can jeopardize the DQE results in X-ray application. A method to quantify this pattern is the Vertical Dark Signal Non-Uniformity (DSNU) as described by EMVA 1288 3.1 standard [37]. This method can be understood as a vertical Fourier transform that will peak at spatial frequencies corresponding to cyclic lines patterns. As expected, the vertical DSNU showed a clear peak corresponding to the pattern spatial frequency in visible light (FIG 20, red curve).
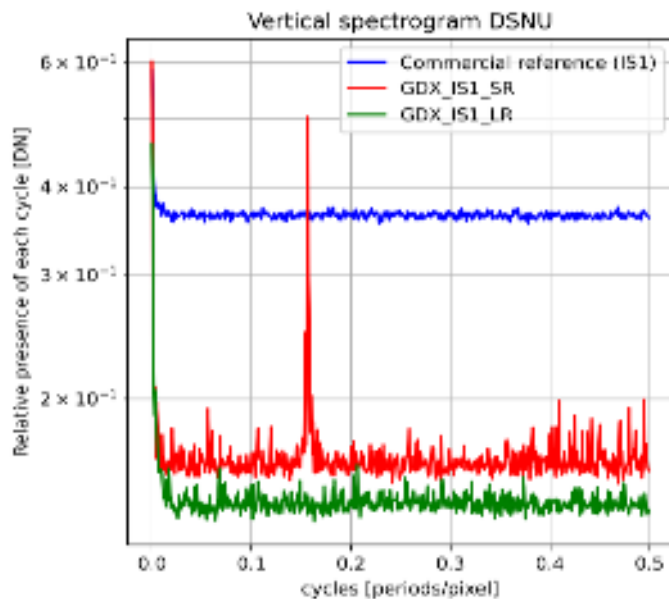
FIG 20. Dark Signal Non-Uniformity (DSNU) (bottom) plots from the developed GDX_IS1_LR (Red) and GDX_IS1_SR (Green) multi-camera modules and the reference commercial camera with IS1 sensor (Blue).

A second Multi-camera module (GDX_IS1_LR) was developed to reduce the high noise levels observed in the first module, maintaining the same architecture but using linear voltage regulators instead of switching voltage regulators. Replacing the voltage regulators highly reduced the observed linear pattern and its frequency peak (FIG 20, green curve). This improved the resulting SNR (FIG 21, green), leading to a similar SNR levels to the reference commercial camera (FIG 21, blue).
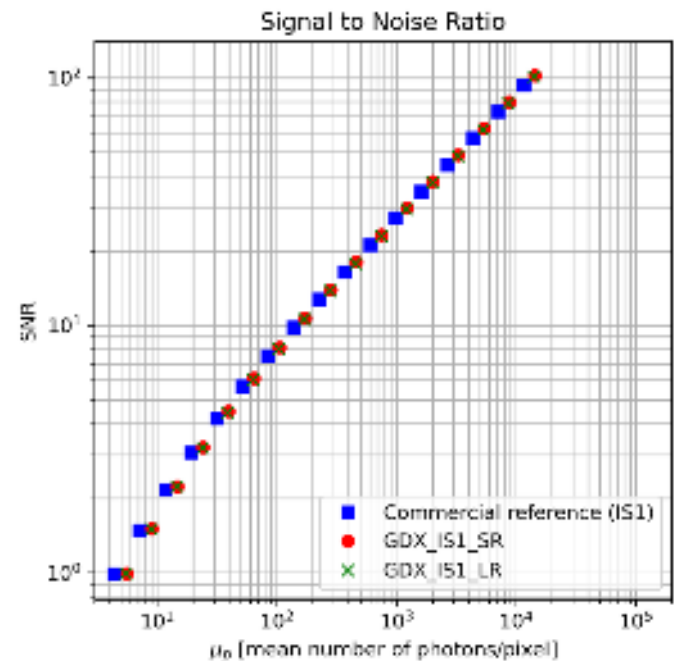
FIG 21. Signal to Noise Ratio (SNR) plots from the developed GDX_IS1_LR (Red) and GDX_IS1_SR (Green) multi-camera modules and the reference commercial camera with IS1 sensor (Blue).

C. Temperature and humidity influence

To determine temperature and humidity influence on the developed multi-camera module, the visible light characterization was repeated with the detector inside a climatic chamber under multiple controlled temperature and relative humidity conditions (the whole test setup including light source and integrating sphere was also mounted inside the climatic chamber). The measurements were done at 25°C (<20% RH), 50°C (<20% RH), 50°C (>90% RH) and compared to the measurement results at room conditions. In order to maintain the exact environmental conditions during all the stages of the light characterization measurements, it was decided not to open

the chamber to place the sensor cover for the dark images measurement. Thus, the dark images measurements were done under the climatic chamber darkness conditions.

The results show no significant degradation of the signal to noise ratio (FIG 22 (top)). The vertical spectrogram of dark signal non-uniformity (FIG 22 (bottom)) exhibits no specific artifacts under the variation of the climatic conditions. Curves corresponding to measurement into climatic chamber (FIG 22 (bottom), Blue, Red, and Cyan) have an offset compared to the reference measurement at room conditions (FIG 22 (bottom), Green). This was caused by the imperfect darkness conditions inside the climatic chamber.
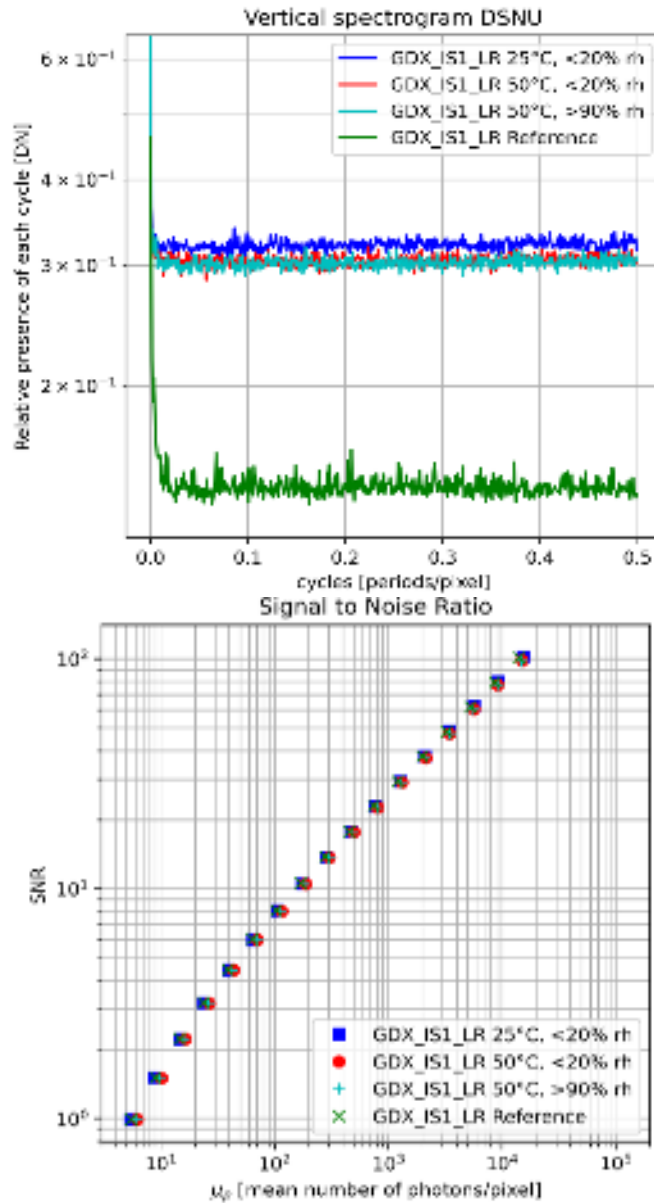
FIG 22. Signal to Noise Ratio (SNR) (top) and Dark Signal Non-Uniformity (DSNU) (bottom) plots from the developed GDX_IS1 multi-camera modules at room conditions (Green), 25°C and <20% RH (Blue), 50°C and <20% RH (Red), 25°C and >90% RH (Cyan).

D.   X-ray characterization

The developed detector was characterized with the two most promising scintillators identified during the characterization phase, i.e. the SC1(CI) (CsI:Tl) and the SC5(GOS) (Gd_2O_2S:Tb). The DQE was measured for different DAK, between 0.59 and 20 µGy peak (0.63 to 20 mAs) at the detector for the RQA5 beam (70 kV), at a frequency of 0.5 mm^{-1} (FIG 23). The low-frequency fixed pattern noise on the images increased the NPS and decreased the DQE below 0.5 mm^{-1}. The best performance for the developed detector was observed between 0.5 and 5.0 uGy at the detector. The maximal DQE for the SC1(CI) and SC5(GOS) scintillators were around 0.60 and 0.30, respectively, for the reference DAK chosen at 2.34 µGy. The fixed pattern noise increases with the DAK squared and make the low-frequency DQE decreases as a function of the DAK.

The higher DQE obtained with the SC1(CI) scintillator can be explained by its micro-pillar structure and high thickness: CsI:Tl is a crystal that can be grown in vertical micro-pillars structures (2-5 um diameter, and over 400 um long) on a plane surface. This helps guiding the light in one direction and avoid lateral scattering, therefore, the MTF is generally better in CsI:Tl scintillators. Gd_2O^2S:Tb is deposited in a powder structure and therefore has no light guiding capability, which leads to wide-angle scattering of the visible photons and lower image sharpness [54].
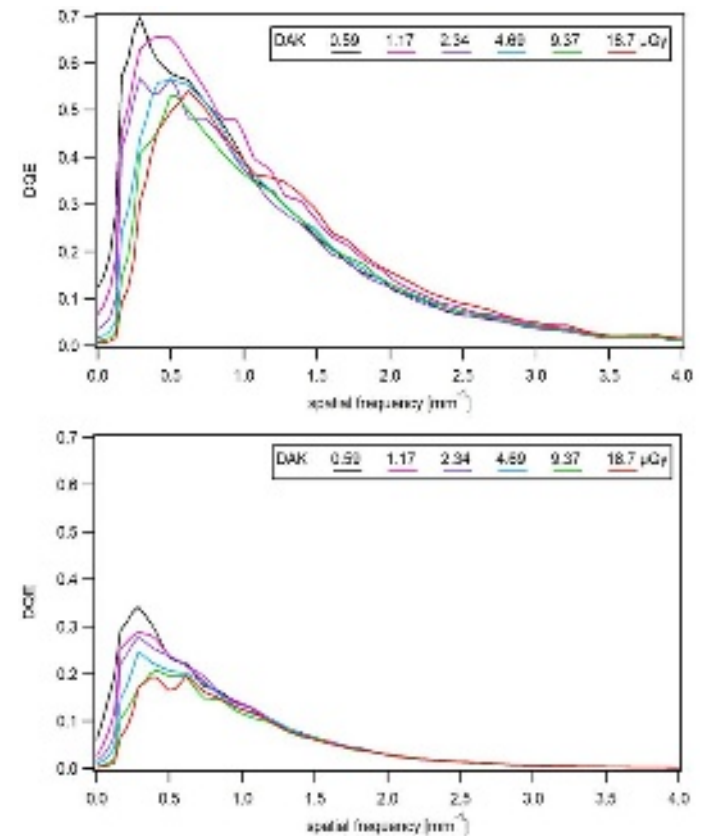
FIG 23. DQE curves obtained with the developed detector (GDX_IS1_LR) at different DAK. The top plots were obtained with the SC1(CI) Scintillator and the ones in the bottom with the

SC5(GOS) scintillator .

The light throughput of the scintillator depends on the conversion efficiency for a given X-ray radiation. It is linked to the absorption rate and light yield (also called gain). For a given thickness, CsI:Tl has higher absorption rate and light yield compared to $Gd_2O_2S:Tb$. Therefore, the light throughput of CsI:Tl scintillators is higher [55]. Nevertheless, these performances have a cost. Due to its manufacturing complexity (crystal growth) that requires complex and expensive facilities, CsI:Tl scintillators are more expensive than $Gd_2O_2S:Tb$, especially for large area (e.g. 430 mm by 430 mm). Moreover, contrary to CsI:Tl, $Gd_2O_2S:Tb$ has very good chemical durability, mechanical properties, uniformity and is easier to manufacture [56].

In sum, compared to the SC1(CI) scintillator, the lower X-ray capture efficiency and X-rays to light photons conversion rate of the SC5(GOS) scintillator decrease the low-frequency DQE. The CsI needles of the SC1(CI) scintillator channel the light photons and avoid light spread that occurs in the grain structure of the SC5(GOS). Light spread decreases the spatial resolution and the high-frequency DQE of the SC5(GOS) scintillator.

VI. CONCLUSIONS

A novel, robust and low cost X-ray imaging system was developed, adapted to the needs and constraints of LMICs. The developed system is based on an indirect conversion chain: a scintillator plate produces visible light when excited by the X-rays then a matrix of the developed multi-camera modules converts the visible light from the scintillator into a set of digital images. The partial images are then unwarped, enhanced and stitched by a specialized software running on a network of FPGAs controlled by a master unit. By implementing a network of FPGA units (instead of a single more powerful processing unit), the partial images can be processed in parallel, reducing the total processing time. Different commercially available components were characterized and the most suitable were implemented in the fabrication of the detector.

The developed system was characterized at the Institute of Radiation Physics (IRA) from the Lausanne University Hospital (CHUV) using different standard medical radiology measurement setups. The characterization measurements of the developed detector led to high quality X-ray images with DQE levels up to 60% (@ 2.34 μGy).

The developed detector was designed to overcome common issues of currently available X-ray detectors in LMICs identified during our field (and literature) study. Amongst the advantages of the developed detector are: Robustness: The detector was designed to withstand the harsh environmental conditions of tropical countries. The characterization results at high temperature (50°C) and humidity (>90% RH) conditions did not show any significant degradation of the signal to noise ratio. Low cost: The use of "off the shelf" components has the advantage of state of the art technologies at a lower cost than customized components. The fabrication costs of the developed detector are between 20 to 50% lower than the flat panel solutions available in the market today; and it is expected that, if mass-produced, the costs will decrease further. Modularity: The implemented modular design allows the system to be easily repaired (by simple replacement of individual modules) without the need of high technical expertise. Additionally, by using "off the shelf" components, the replacement parts can be easily obtained in the market and be replaced at a low costs, i.e. in the range of hundreds of USD. Conversely, when the detector from a traditional digital X-ray device breaks it must be replaced completely by specialized personnel at a high costs, i.e. in the range of tens of thousands USD.

However, these advantages come with a cost: due to the lower optical coupling of the implemented architecture, the DQE levels of the developed detector are around 15% lower than the flat panel solutions, i.e. the average DQE levels for commercial flat panels are around 70% (CsI:Tl) and 35% ($Gd_2O_2S:Tb$) while the DQE levels measured with our detector are 60% (CsI:Tl) and 30% ($Gd_2O_2S:Tb$). Nevertheless, the measured DQE levels are much higher than other multi-camera systems available in the market (The DQE levels for characterized commercial multi-camera detectors with CsI:Tl are between 30 to 40%) and the film based X-ray systems, predominant in low income countries (the DQE levels of film bases systems are ≤25% [57,58]). Therefore, the developed X-ray detector shows very promising results and potential for being implemented in the context and harsh environmental conditions of LMICs at a lower purchasing and maintenance costs than traditional digital X-ray detectors.

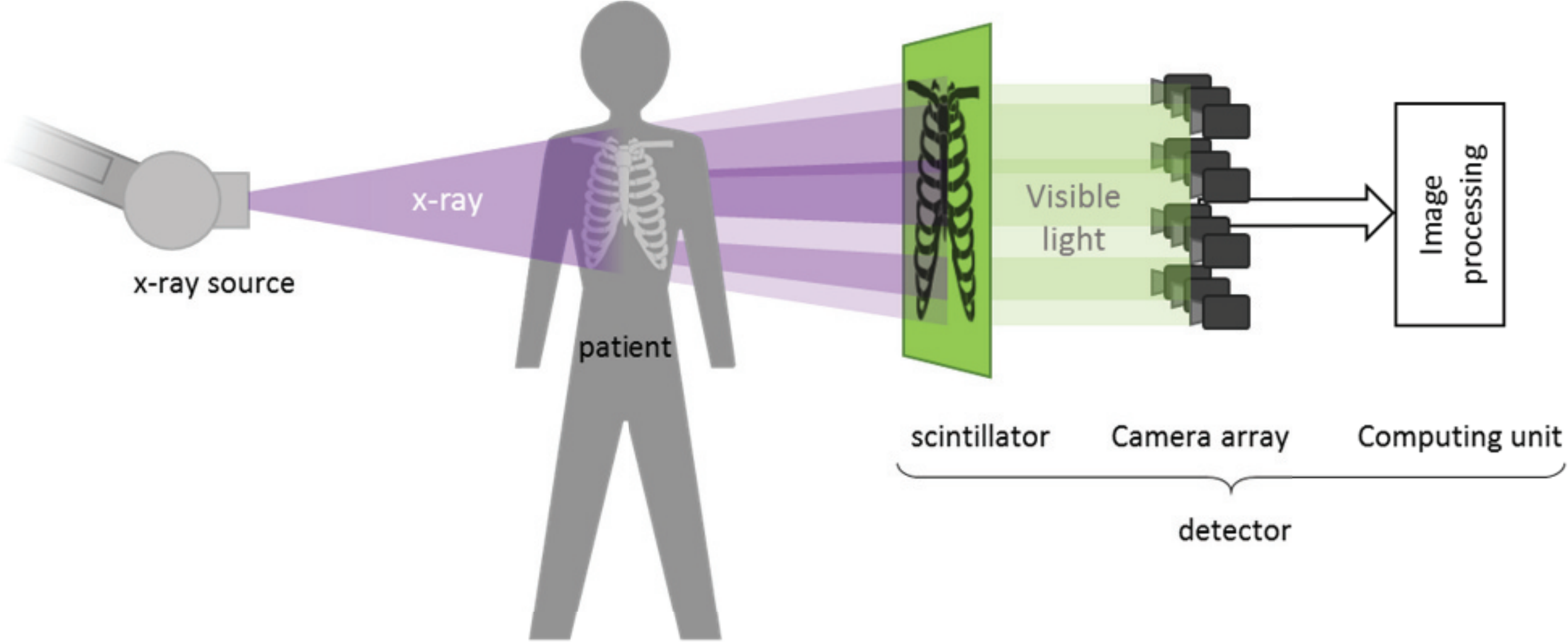## ACKNOWLEDGMENTS

DATA AVAILABILITY STATEMENT

The data that support the findings of this study are available from the corresponding author upon reasonable request.
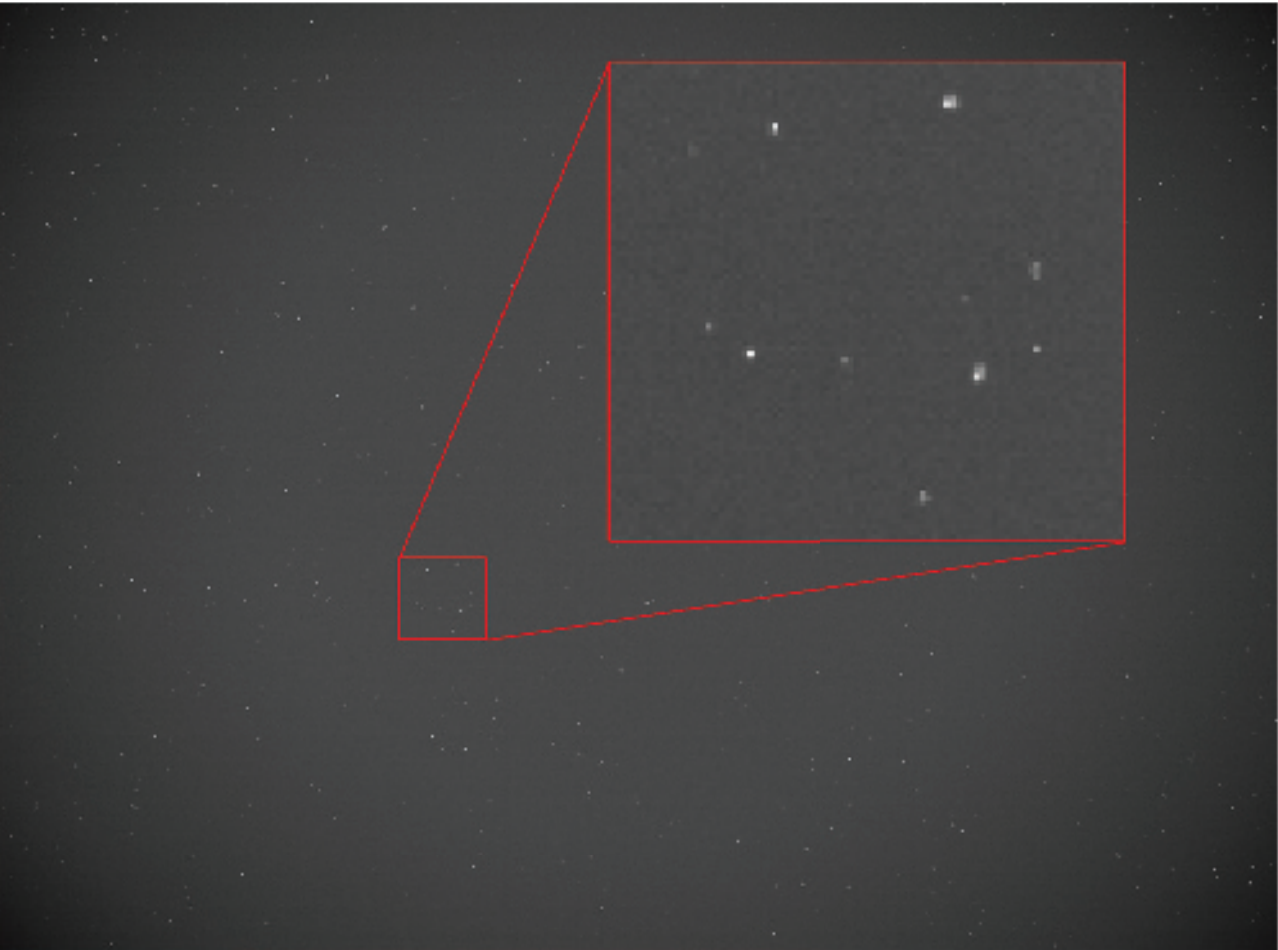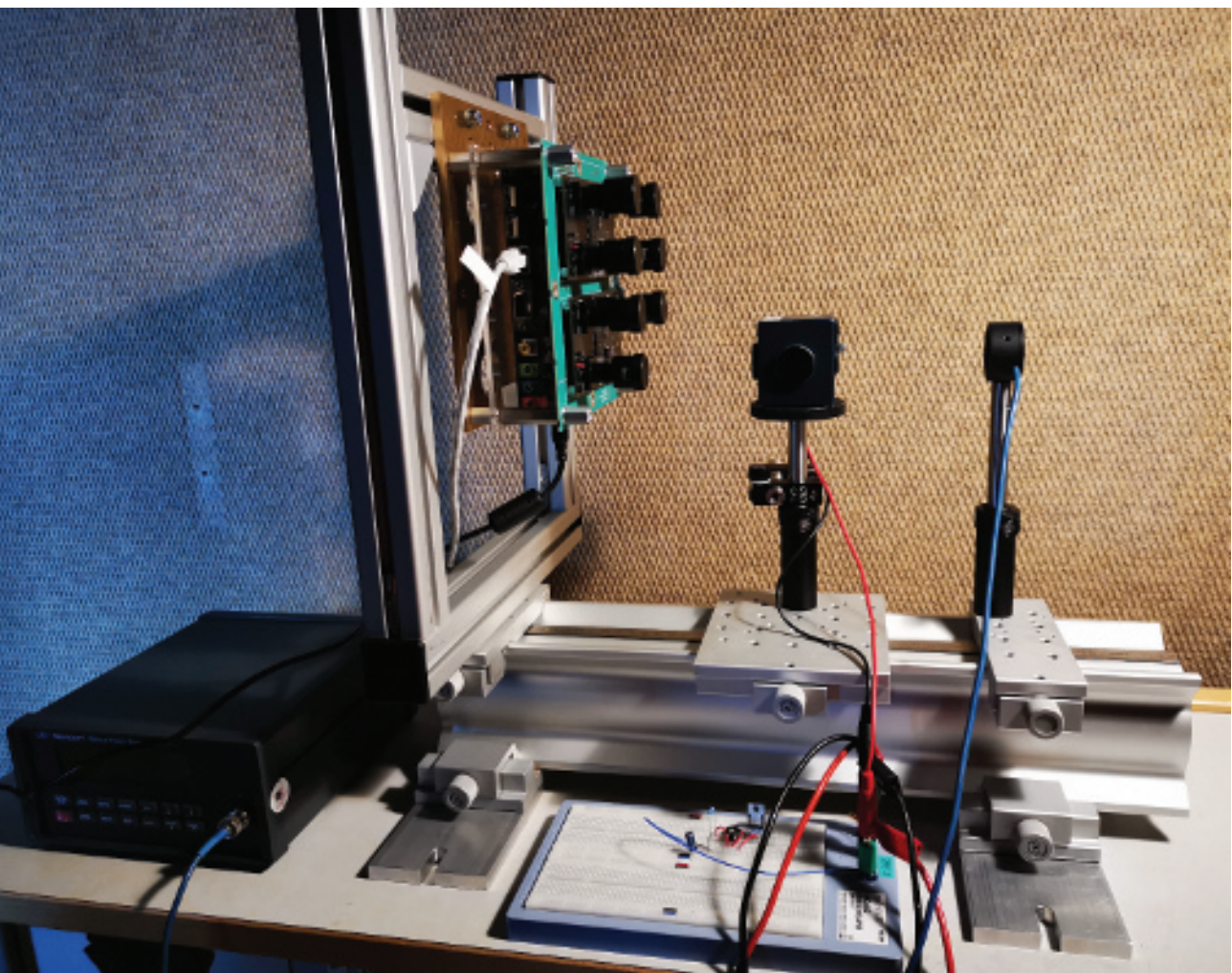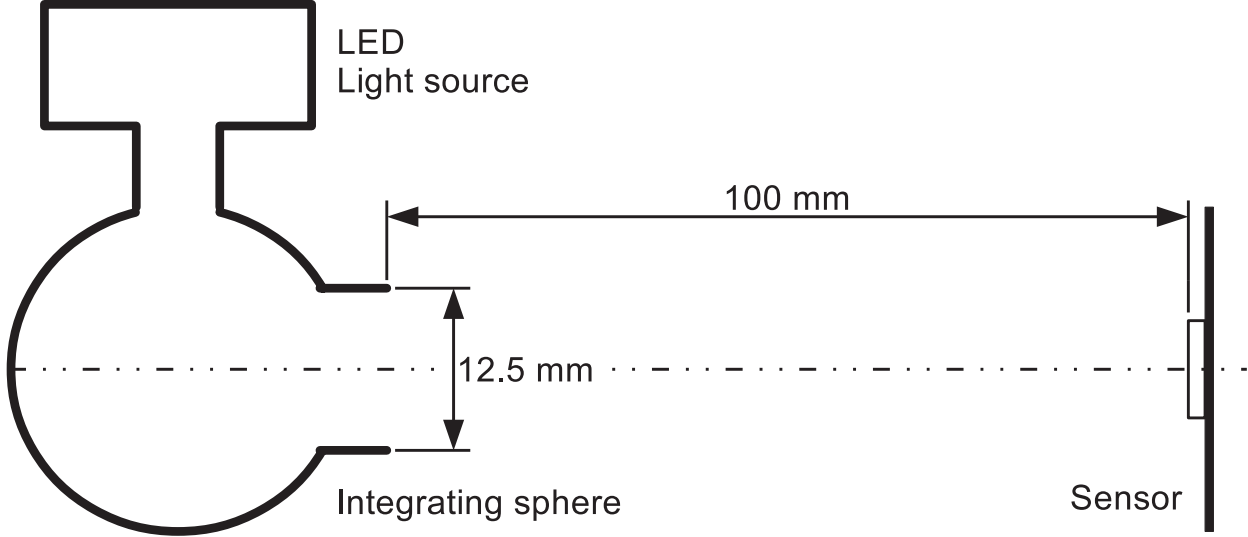
REFERENCES

[1] PAHO-WHO. World Radiography Day: Two-Thirds of the World's Population has no Access to Diagnostic Imaging. 2012. [cited 2020 September]. Available from: https://www.paho.org/hq/index.php?option=com_content&view=article&id=7410:2012-dia-radiografia-dos-tercios-poblacion-mundial-no-tiene-acceso-diagnostico-imagen&Itemid=1926&lang=en

[2] Silverstein, J. Most of the World Doesn't Have Access to X-Rays. The Atlantic. 2016

[3] Mollura DJ, Lungren MP. (2014). *Radiology in Global Health: Strategies, Implementation and Applications*. Springer-Verlag New York. p.19. ISBN 978-1-4614-0603-7

[4] Racoveanu, N.T. Medical imaging in the new millennium. How has worldwide health care benefited?. EMHJ - Eastern Mediterranean Health Journal, 8 (1), 192-204. 2002.

[5] International Atomic Energy Agency. Worldwide Implementation of Digital Imaging in Radiology: A Resource Guide. IAEA Human Health Series No. 28. Vienna, 2015.

[6] Marks, I.H., et al. Medical equipment donation in low-resource settings: a review of the literature and guidelines for surgery and anaesthesia in low-income and middle-income countries. BMJ Global Health 2019; 4:e001785.

[7] Inglin, S. (Producer & Director), EssentialMed Foundation (Co-producer). "X-Ray Machines: Africa's Broken System", (2019). [Video file]. Accessed on: Aug. 5, 2021[Online]. Available: https://essentialtech.center/x-ray-machines-africas-broken-system/

[8] Makohliso, S., Klaiber, B., Sahli, R., Tapouh, J. R. M., Amvene, S. N., Stoll, B., & Schönenberger, K. Medical technology innovation for a sustainable impact in Low- and Middle-Income countries: a holistic approach. 2020, July 4. https://doi.org/10.31224/osf.io/2dytg

[9] Norman, D., Spencer, E. COMMUNITY-BASED, HUMAN-CENTERED DESIGN". jnd.org (1 January 2019). Accessed on: Aug. 6, 2021[Online]. Available: https://jnd.org/community-based-human-centered-design/

[10] Chavarria, M. A. , Mugeere, A. , Schönenberger, K., Hurst, S., Rivas Velarde, M. "Design Approaches for Creating Person-Centered, Context-Sensitive, and Sustainable Assistive Technology for Personal Mobility in the Global South". In J. Lazar & M. Stein (Eds.), "Accessible Technology and the Developing World". 2021.

[11] Shonengerger, K. & Makohliso, S. "Technology Innovation for Sustainable Development". edX. Accessed on: Aug. 6, 2021 [Online]. Available: https://learning.edx.org/course/course-v1:EPFLx+Innov4DevX+1T2017/home

[12] Nickoloff, E. AAPM/RSNA Physics Tutorial for Residents: Physics of Flat-Panel Fluoroscopy Systems. RadioGraphics. 2011. 31 (2): 591–602. doi:10.1148/rg.312105185

[13] Konstantinidis, A. et al. The Dexela 2923 CMOS X-ray detector: A flat panel detector based on CMOS active pixel sensors for medical imaging applications. Nuclear Instruments and Methods in Physics Research A 689 (2012) 12–21.

[14] Bick, U., Diekmann, F. (Eds.), Digital Mammography, Springer, Berlin, 2010.

[15] Varex Imaging. Medical Flat Panel Detectors. Accessed on: Aug. 5, 2021[Online]. Available: https://www.vareximaging.com/products/medical/medical-flat-panel-detectors

[16] Hamamatsu. X-ray flat panel sensors for radiology. Accessed on: Aug. 5, 2021 [Online]. Available: https://www.hamamatsu.com/eu/en/product/optical-sensors/image-sensor/x-ray-flat-panel-sensor/x-ray-flat-panel-sensors-for-radiology/index.html

[17] Smith, C.R., Erker, J.W. "Low-cost, high-resolution x-ray detector system for digital radiography and computed tomography," Proc. SPIE 2009, X-Ray Detector Physics and Applications II, (16 December 1993); doi: 10.1117/12.164751

[18] Cha, B. et al. Performance studies of a monolithic scintillator-CMOS image sensor for X-ray application. Netherlands. 2008. doi:10.1016/j.nima.2008.03.034.

[19] Gelinck, G.H. et al., "X-Ray Detector-on-Plastic With High Sensitivity Using Low Cost, Solution-Processed Organic Photodiodes," in IEEE Transactions on Electron Devices, vol. 63, no. 1, pp. 197-204, Jan. 2016, doi: 10.1109/TED.2015.2432572.

[20] Kim, H.K. et al. "Development and evaluation of a digital radiographic system based on CMOS image sensor," in IEEE Transactions on Nuclear Science, vol. 48, no. 3, pp. 662-666, June 2001, doi: 10.1109/23.940143.

[21] Kim H.K. et al. Development of a lens-coupled CMOS detector for an X-ray inspection system. Nuclear Instruments and Methods in Physics Research A 545 (2005) 210–216.

[22] JPI Healthcare Solutions. IONA Digital X-Ray PSA Detector Datasheet. Accessed on: Aug. 5, 2021 [Online]. Available: https://www.jpihealthcare.com/wp-content/uploads/2017/05/IONA_A4_EN_v4_JPI-Healthcare_Website.pdf

[23] JPI Healthcare Solutions. IONA2 Digital X-Ray PSA Detector Datasheet. Accessed on: Aug. 5, 2021 [Online]. Available: http://www.jpihealthcare.com/wp-content/uploads/2017/05/IONA2_website.pdf

[24] Maidment, A. & Yaffe, M. Analysis of the spatial-frequency-dependent DQE of optically coupled digital mammography detectors. Medical Physics, 1994. 21, 721.

[25] Flynn, M. et al. QuantumNoise inDigitalX-ray ImageDetectors with Optically Coupled Scintillators. IEEE Transactions on Nuclear Science, 1996, vol. 43, issue 4, pp. 2320-2325.

[26] Jing, Z. et al. Detective quantum efficiency of a CsI:T1 scintillator based scanning slot xray detector for digital mammography. In proceeding SPIE on Physics of Medical Imaging, 1998, Vol. 3336. San Diego, California.

[27] Rf system lab. NAOMI X-ray Sensor Specifications. Accessed on: Aug. 5, 2021 [Online]. Available: http://rfsystemlab.com/en/product/medical/naomi/index.html

[28] Weather Atlas. Monthly weather forecast and climate. Accessed on: Aug. 5, 2021[Online]. Available: https://www.weather-atlas.com/en/climate

[29] Arizona State University. WMO Region I (Africa): Highest Temperature. World Meteorological Organization's World Weather & Climate Extremes Archive. Accessed on: Aug. 5, 2021[Online]. Available: https://wmo.asu.edu/content/africa-highest-temperature

[30] World Bank Group. Climate change knowledge portal. Accessed on: Aug. 5, 2021[Online]. Available: https://climateknowledgeportal.worldbank.org/country/burkina-faso/climate-data-historical
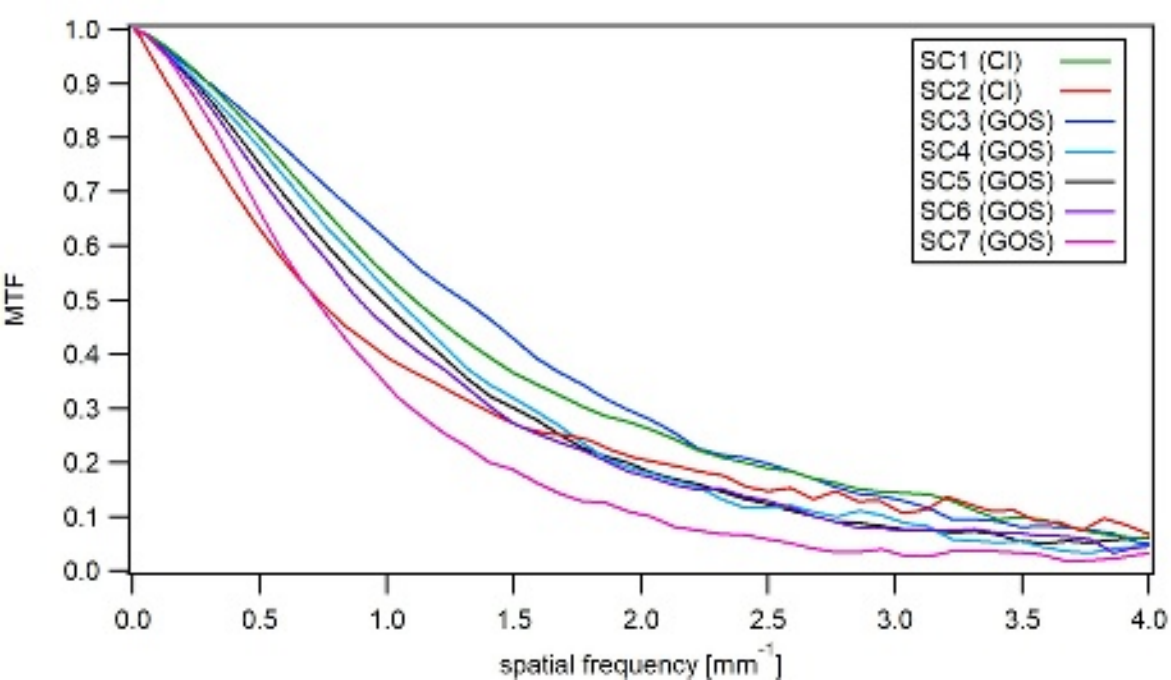
[31] Haddad, M. Mapping the hottest temperatures around the world. Aljazeera. 1 Jul 2021. Accessed on: Aug. 5, 2021[Online]. Available: https://www.aljazeera.com/news/2021/7/1/interactive-mapping-hottest-temperatures-around-world

[32] World Meteorological Organization. World Weather Information Service. Accessed on: Aug. 5, 2021[Online]. Available: https://worldweather.wmo.int/en/city.html?cityId=1514

[33] BBC. BBC weather. Accessed on: Aug. 5, 2021[Online]. Available: https://www.bbc.com/weather/2224827

[34] Leo, W.R. Techniques for Nuclear and Particle Physics Experiments (2nd ed.). 1994. Springer. doi:10.1007/978-3-642-57920-2.ISBN 978-3540572800.

[35] Mikhailik, V.B. Kraus, H. "Scintillators for cryogenic applications; state-of-art". Journal of Physical Studies. 2010. 14 (4): 4201–4206.

[36] Laird Thermal Systems. Thermoelectric Cooling for CMOS Sensors. Laird Thermal Systems Application Note. April, 2019

[37] European Machine Vision Association. "EMVA Standard 1288: Standard for Characterization of Image Sensors and Cameras", Release 3.1, December 30, 2016.

[38] ICRU Report 54 1996 Medical imaging—The assessment of image quality. J ICRU os 28. (10.1093/jicru/os28.1.Report54).

[39] IEC. Medical electrical equipment - Characteristics of digital X-ray imaging devices - Part 1-1: Determination of the detective quantum efficiency - Detectors used in radiographic imaging. IEC 62220-1-1:2015.

[40] Nishikawa, R.M. "The Fundamentals of MTF, Wiener Spectra, and DQE", [cited 2020 September]. Available from: https://www.aapm.org/meetings/99am/pdf/2798-87374.pdf

[41] Cunningham, I. A., Fenster. A. "A method for modulation transfer function determination from edge profiles with correction for finite-element differentiation". Med Phys. . 1987. 14: 533.

[42] Sandrik, J.M., Wagner. R.F. "Absolute measures of physical image quality: Measurement & application to radiographic magnification", Med. Phys. 1982. 9: 540.

[43] Yang, P., et al. "Effect of Humidity on Scintillation Performance in Na and Tl Activated CsI Crystals". April 2014, IEEE Transactions on Nuclear Science 61(2):1024-1031; DOI: 10.1109/TNS.2014.2300471

[44] Saint-Gobain Crystals and Detectors. "Handling and Care of Crystal Scintillation Detectors". Netherlands. [cited 2020 September]. Available from: https://www.crystals.saint-gobain.com/sites/imdf.crystals.com/files/documents/handling-and-care-of-crystal-scintillation-detectors_70413.pdf

[45] Saint-Gobain Crystals and Detectors. "CsI(Tl), CsI(Na) Cesium Iodide Scintillation Material". Netherlands. [cited 2020 September]. Available from: https://www.crystals.saint-gobain.com/sites/imdf.crystals.com/files/documents/csitl-and-na-material-data-sheet.pdf

[46] Carel W E van Eijk. "Inorganic scintillators in medical imaging". Phys. Med. Biol. 2002. 47 P. R89.

[47] Dippel, S. Stahl, M. Wiemker, R. & Blaffert, T. Multiscale contrast enhancement for radiographies: Laplacian pyramid versus fast wavelet transform. IEEE Transactions on medical imaging, 2002.21(4), Pp. 343-353,

[48] Zhang, Z. "A flexible new technique for camera calibration". IEEE Transactions on pattern analysis and machine intelligence, 2000. 22(11), Pp. 1330-1334.

[49] Bradski, G.& Kaehler, A. OpenCV. Dr. Dobb's journal of software tools, 3. 2000.

[50] Oyamada, Y. Fallavollita, P. & Navab, N. "Single camera calibration using partially visible calibration objects based on random dots marker tracking algorithm". In The IEEE and ACM International Symposium on Mixed and Augmented Reality, Workshop on Tracking Methods and Applications (TMA), Atlanta, USA. Nov. 2012.

[51] Brown, M. & Lowe, D.G. "Automatic panoramic image stitching using invariant features". International journal of computer vision, 2007. 74(1), 59-73.

[52] Kwatra, V. Schödl, A. Essa, I. Turk, G. & Bobick. A. "Graphcut textures: image and video synthesis using graph cuts". ACM Transactions on Graphics (ToG), 2003. 22(3), 277-286.

[53] Burt, P.J. & Adelson, E.H. "A multiresolution spline with application to image mosaics". ACM Transactions on Graphics (TOG), 1983. 2(4), 217-236.

[54] Bo, K.C. et Al. "Fabrication and comparison Gd202S(Tb) and CsI(TI) films for X-ray imaging detector application". 2008 IEEE Nuclear Science Symposium Conference Record, NSS/MIC 2008, pp.1232 – 1235.

[55] Farman, T. et Al. "Effects of scintillator on the detective quantum efficiency (DQE) of a digital imaging system". OOOOE. 2006. Vol. 101, 2, Pp. 219-223.

[56] Im Deok Jung, et al. "Flexible Gd2O2S:Tb scintillators pixelated with polyethylene microstructures for digital X-ray image sensors". Journal of Micromechanics and Microengineering, 2009. Volume 19, Number 1.

[57] Willems, P., Soltani, P., Vaessen, B. Image Quality comparison of Digital Radiographic Systems for NDT. In proceeding 15th World Conference on Non-Destructive Testing. 15-21 October 2000, Rome. [cited 2021 September]. Available: https://www.ndt.net/article/wcndt00/papers/idn421/idn421.htm

[58] Spahn M. Flat detectors and their clinical applications. Eur Radiol. 2005 Sep;15(9):1934-47. doi: 10.1007/s00330-005-2734-9. Epub 2005 Apr 2. PMID: 15806363.
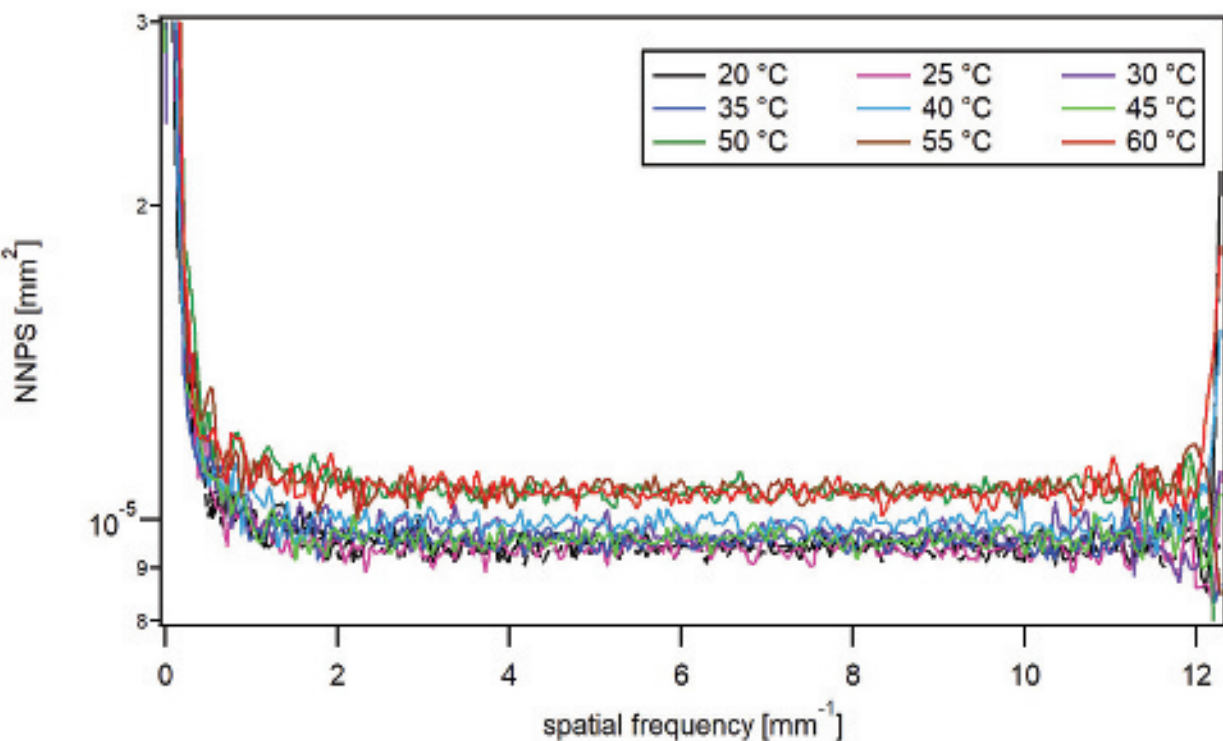
x-ray

x-ray source

patient

Visible light

scintillator   Camera array   Computing unit

Image processing
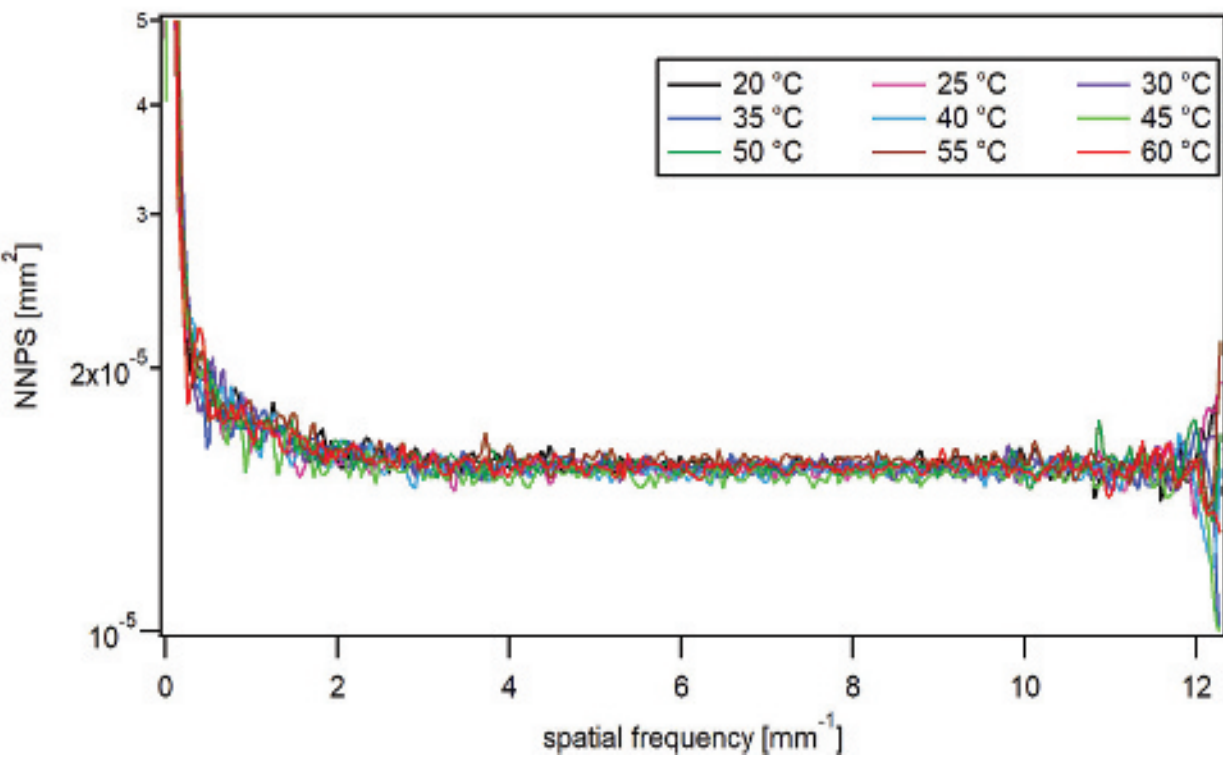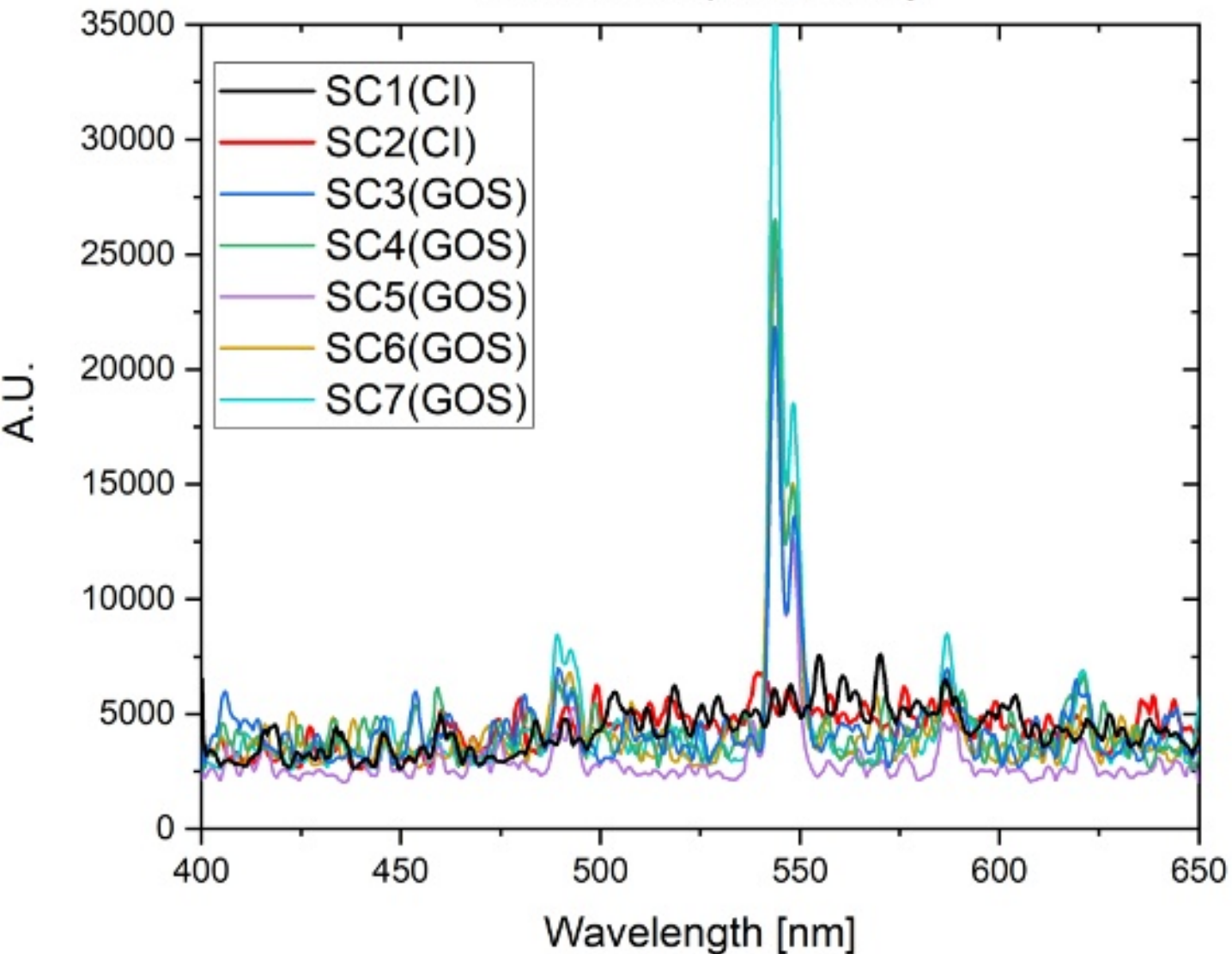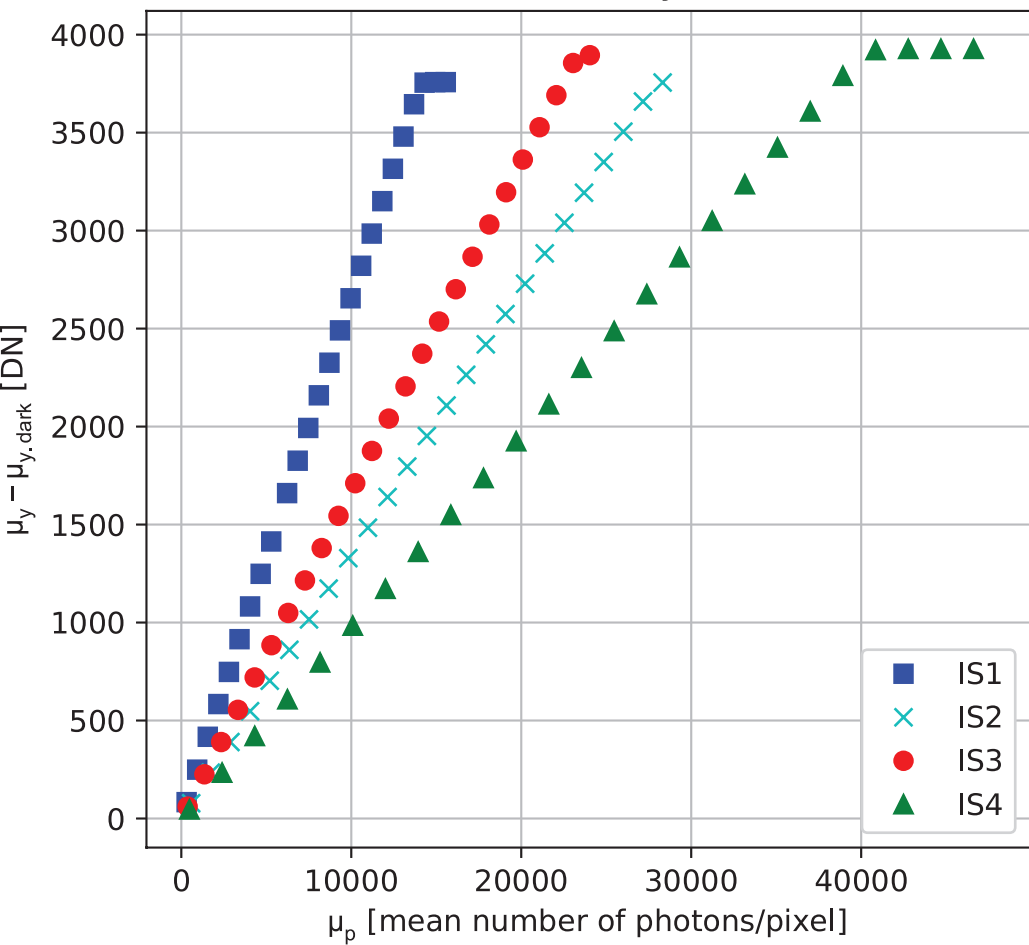
detector

LED Light source

100 mm

12.5 mm

Integrating sphere

Sensor

Scintillator comparison (DQE)

Scintillator Spectrometry
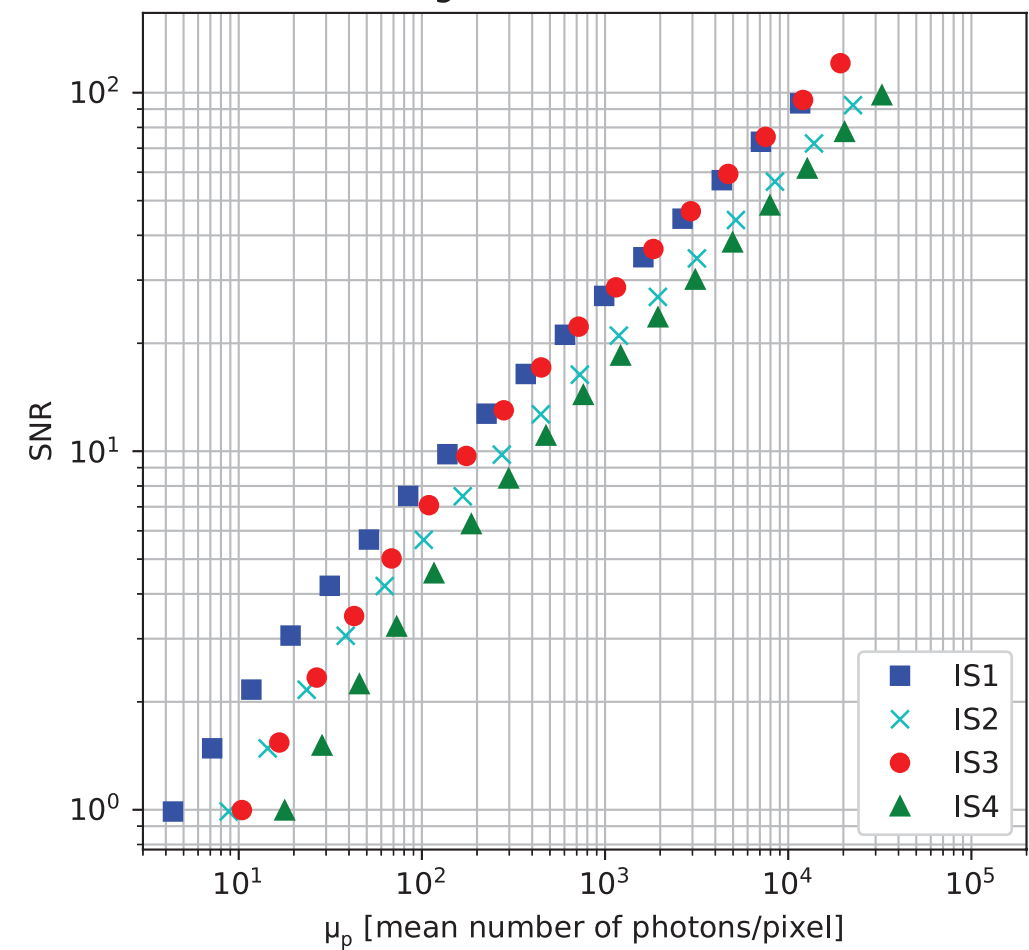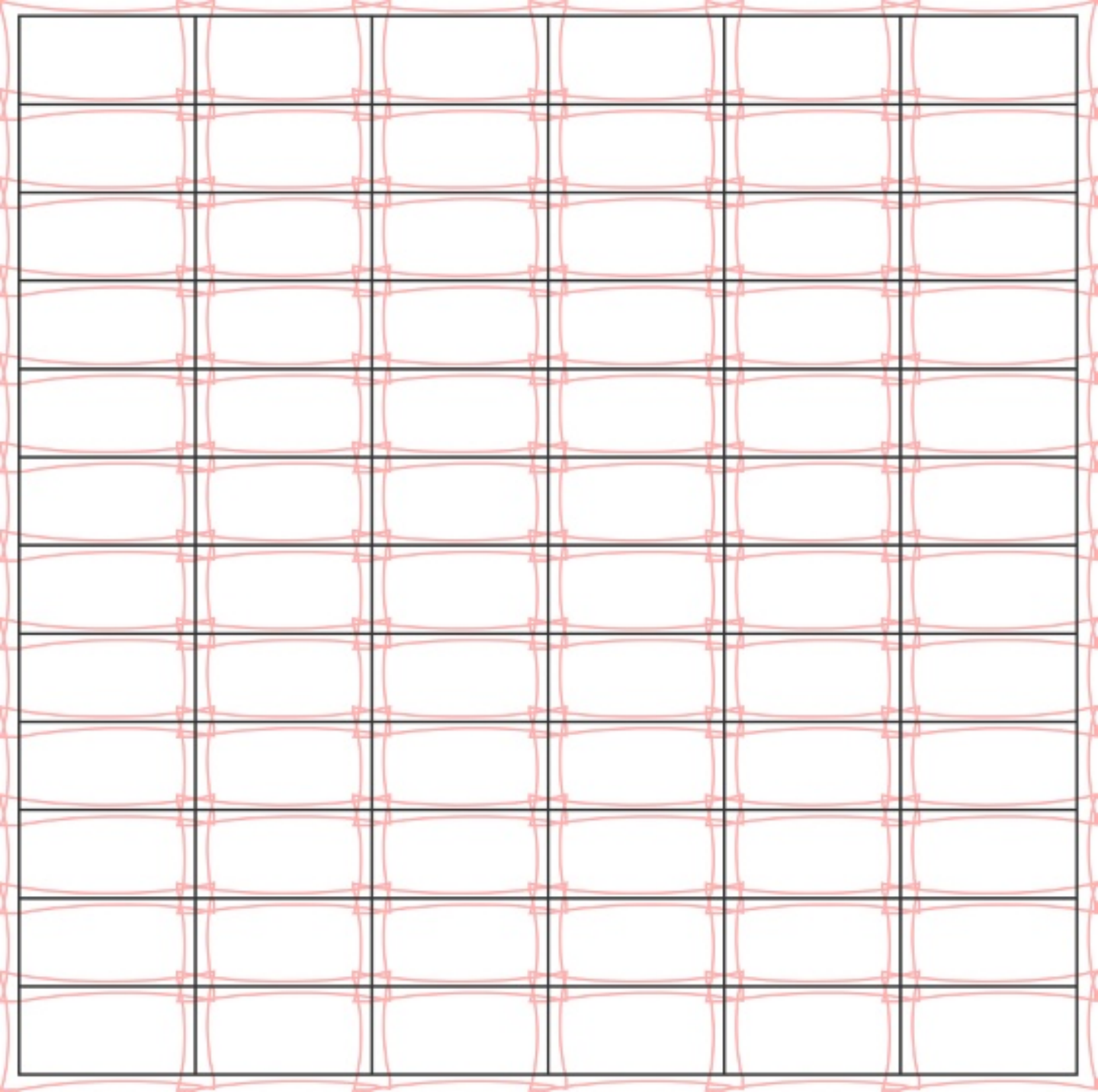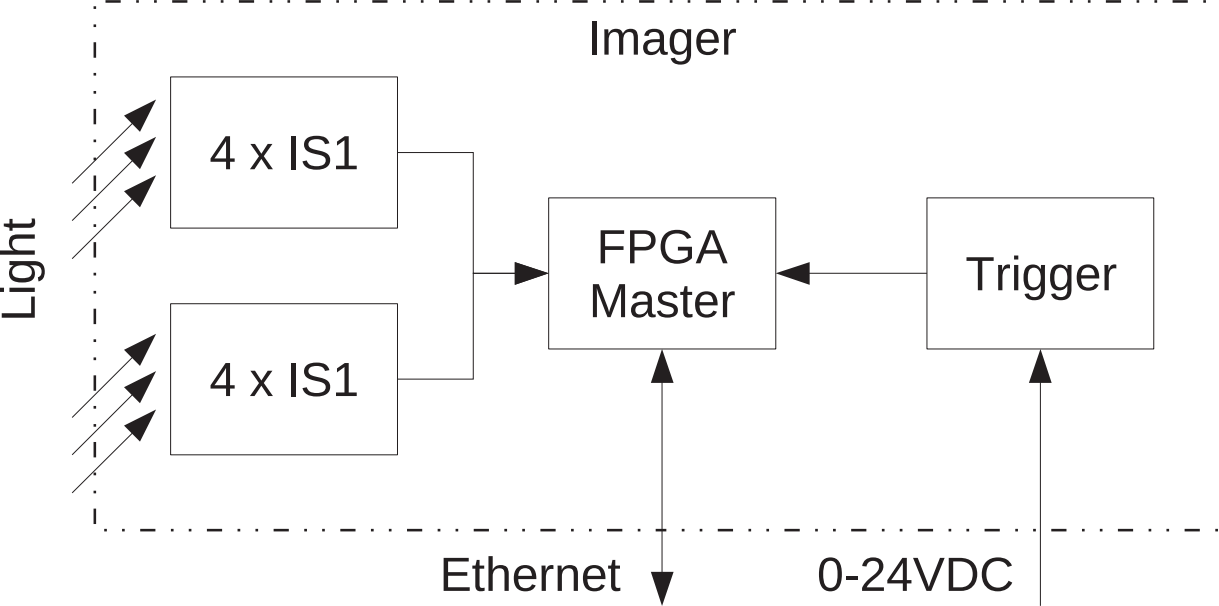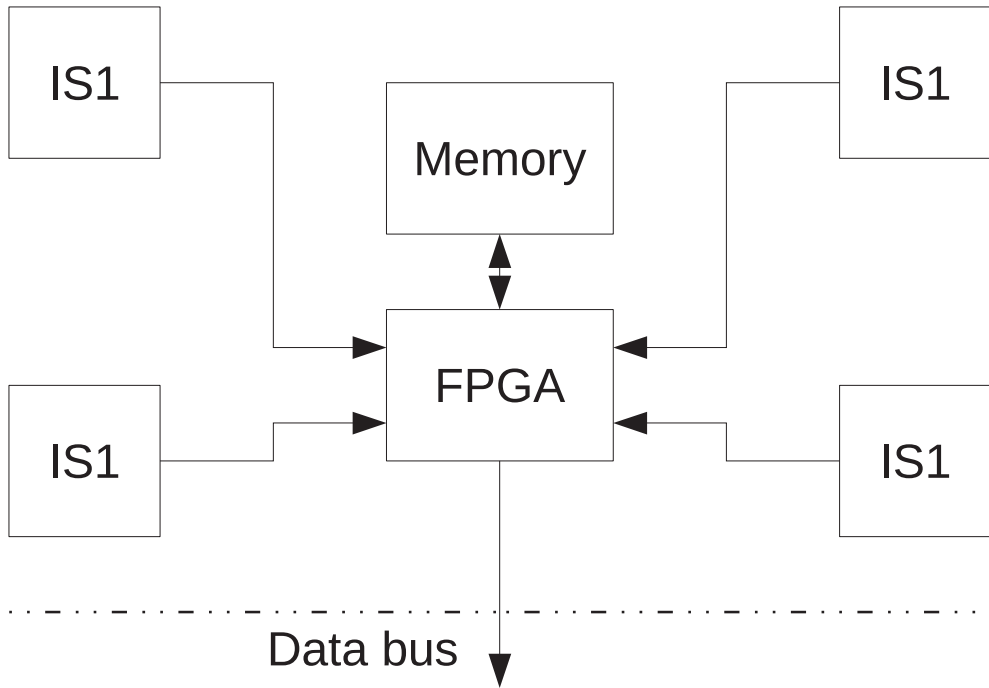
Lens comparison

Sensitivity

$\mu_y - \mu_{y.dark}$ [DN]

μ_p [mean number of photons/pixel]

- IS1
- IS2
- IS3
- IS4

Signal to Noise Ratio

SNR

μ_p [mean number of photons/pixel]

- IS1
- IS2
- IS3
- IS4

Light

Imager

4 x IS1

4 x IS1

FPGA
Master

Trigger

Ethernet

0-24VDC

Imaging module

IS1

IS1

Memory

FPGA
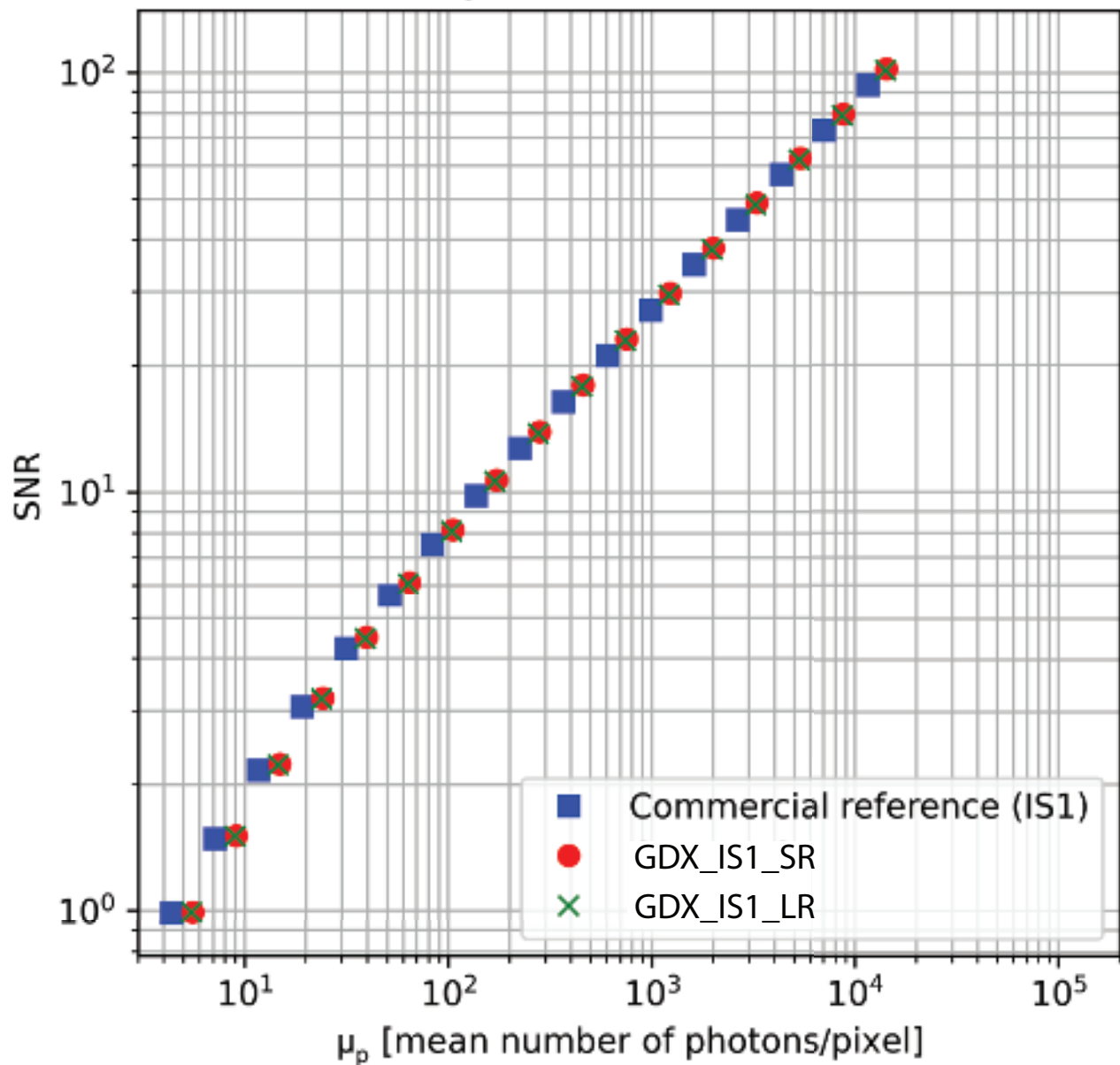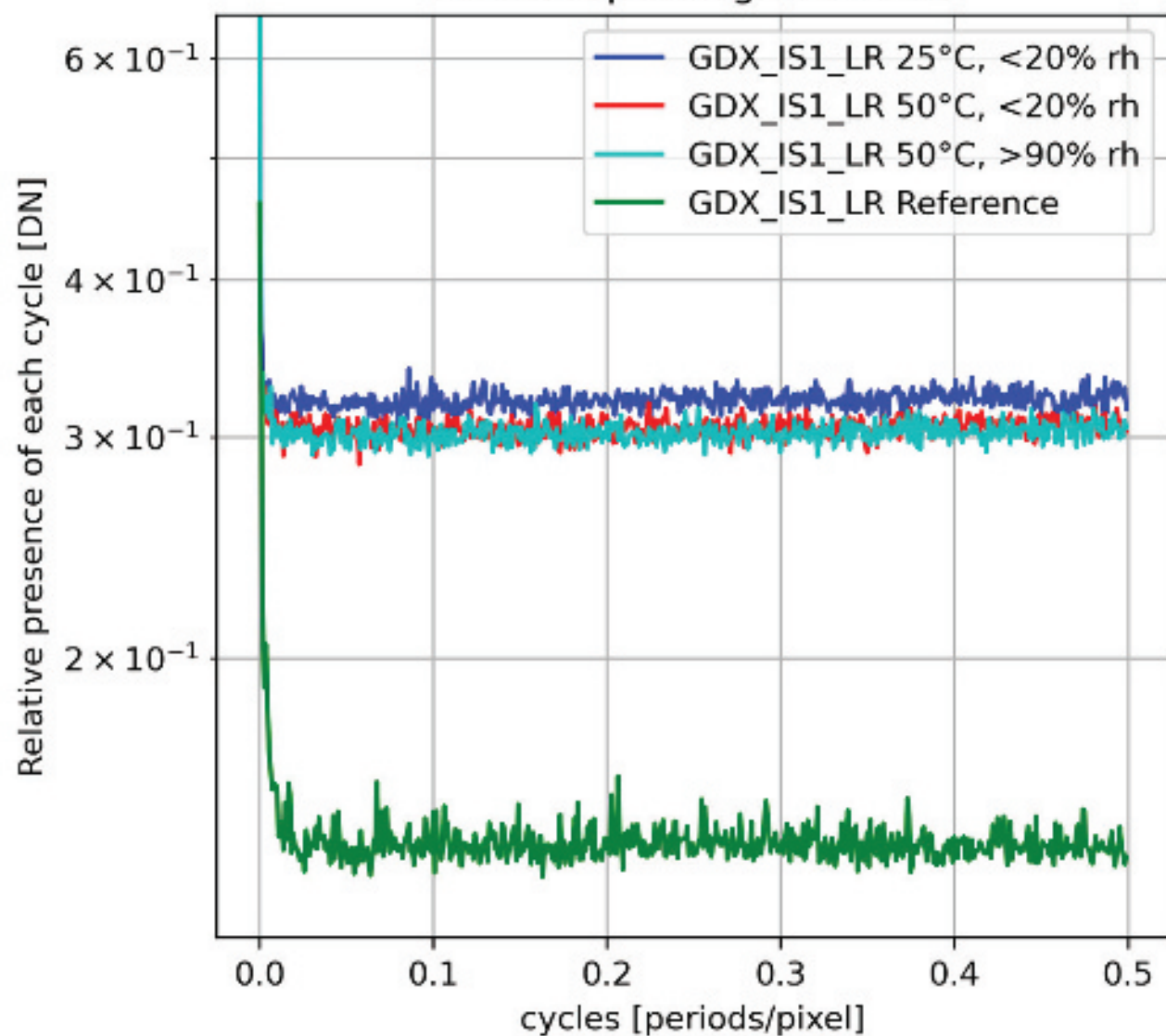
IS1

IS1

Data bus

a) b) c)

a) b) c)
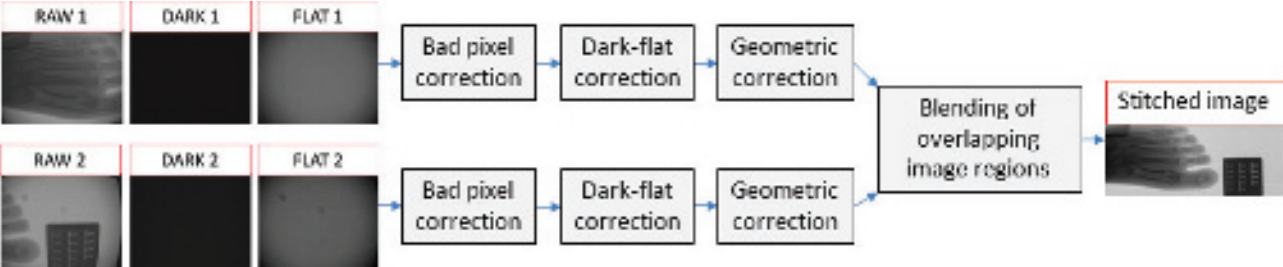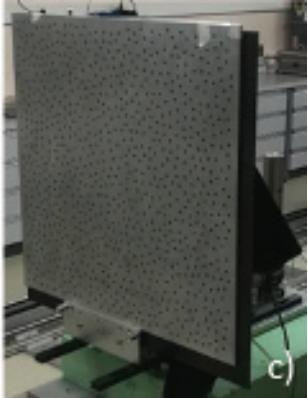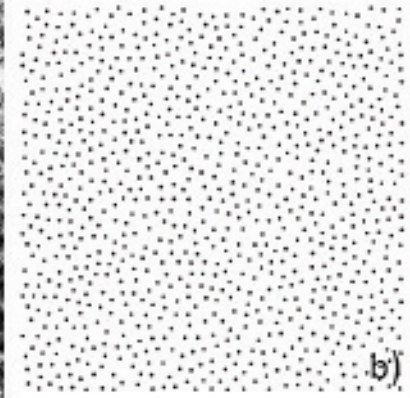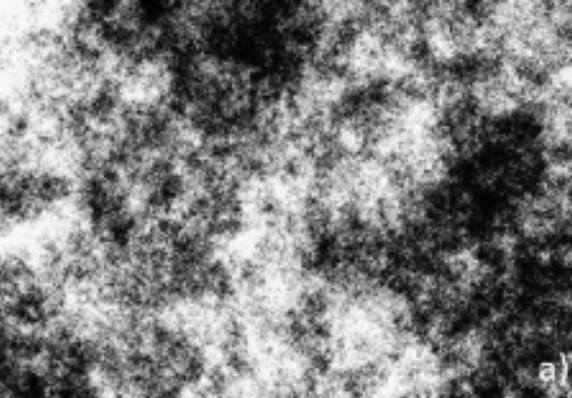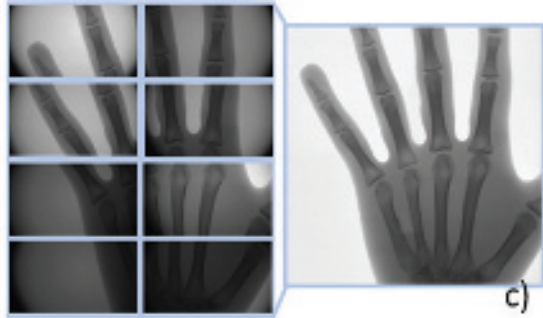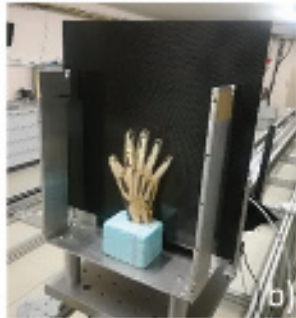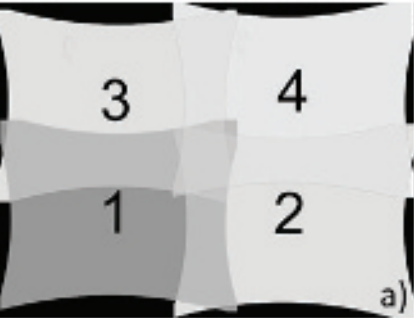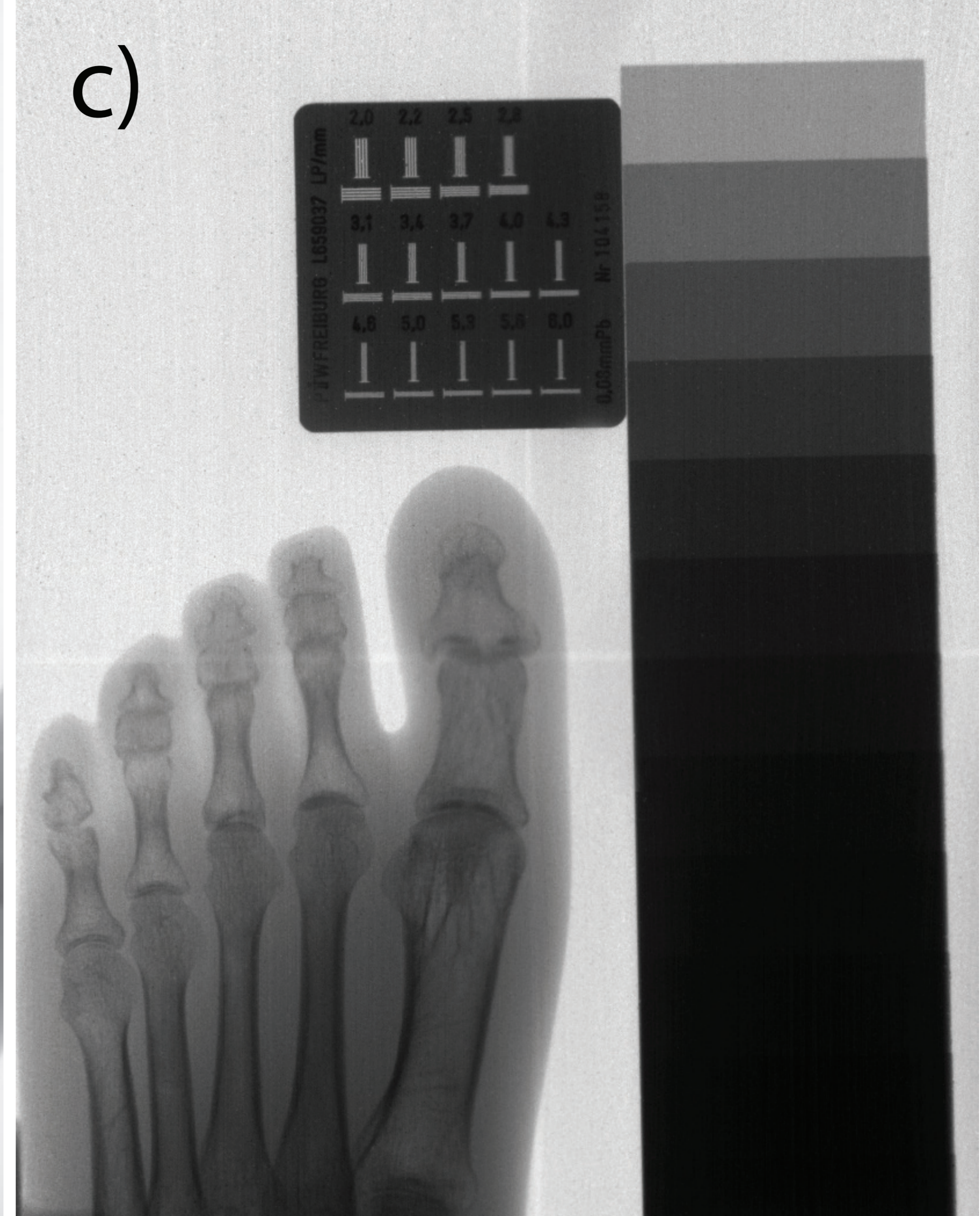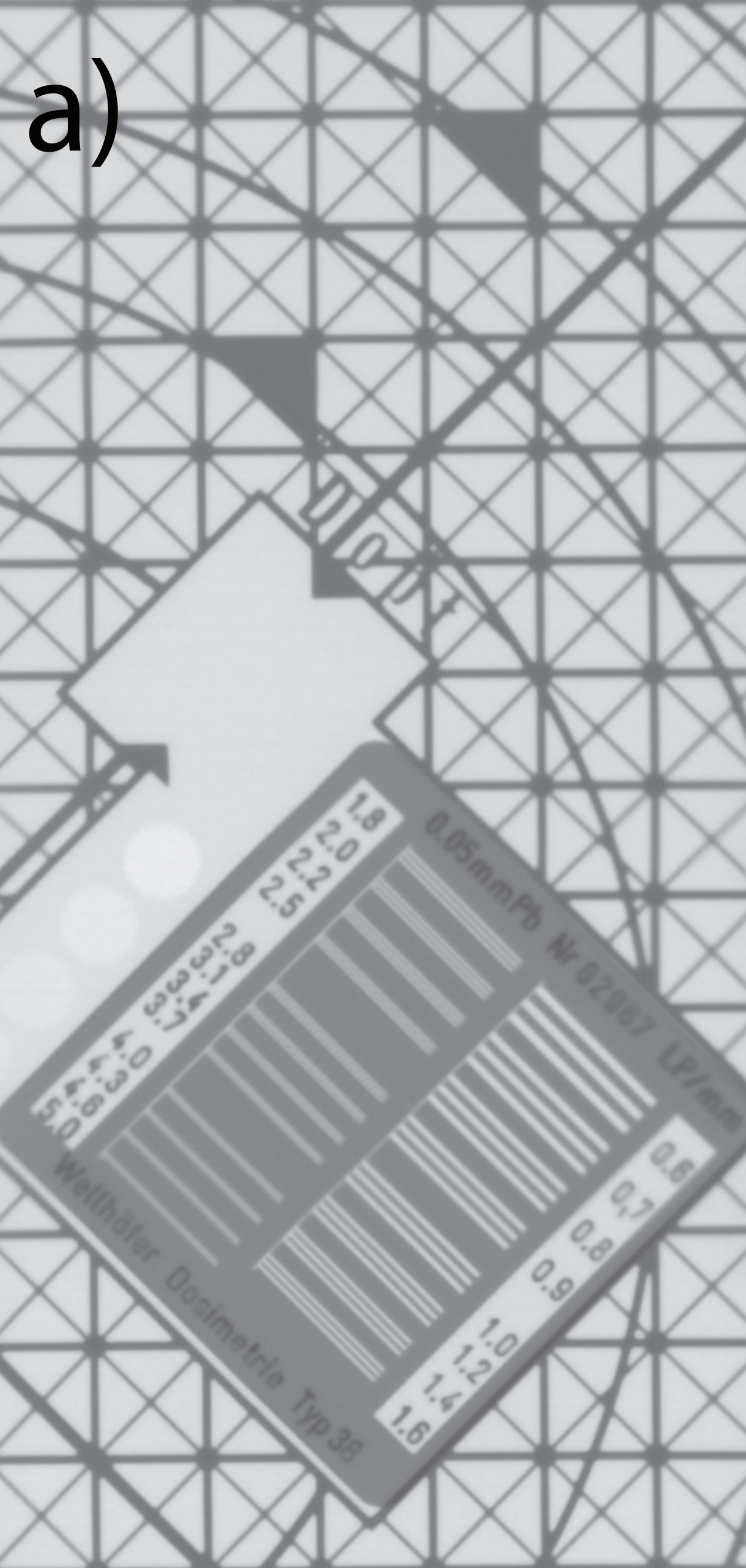
Vertical spectrogram DSNU
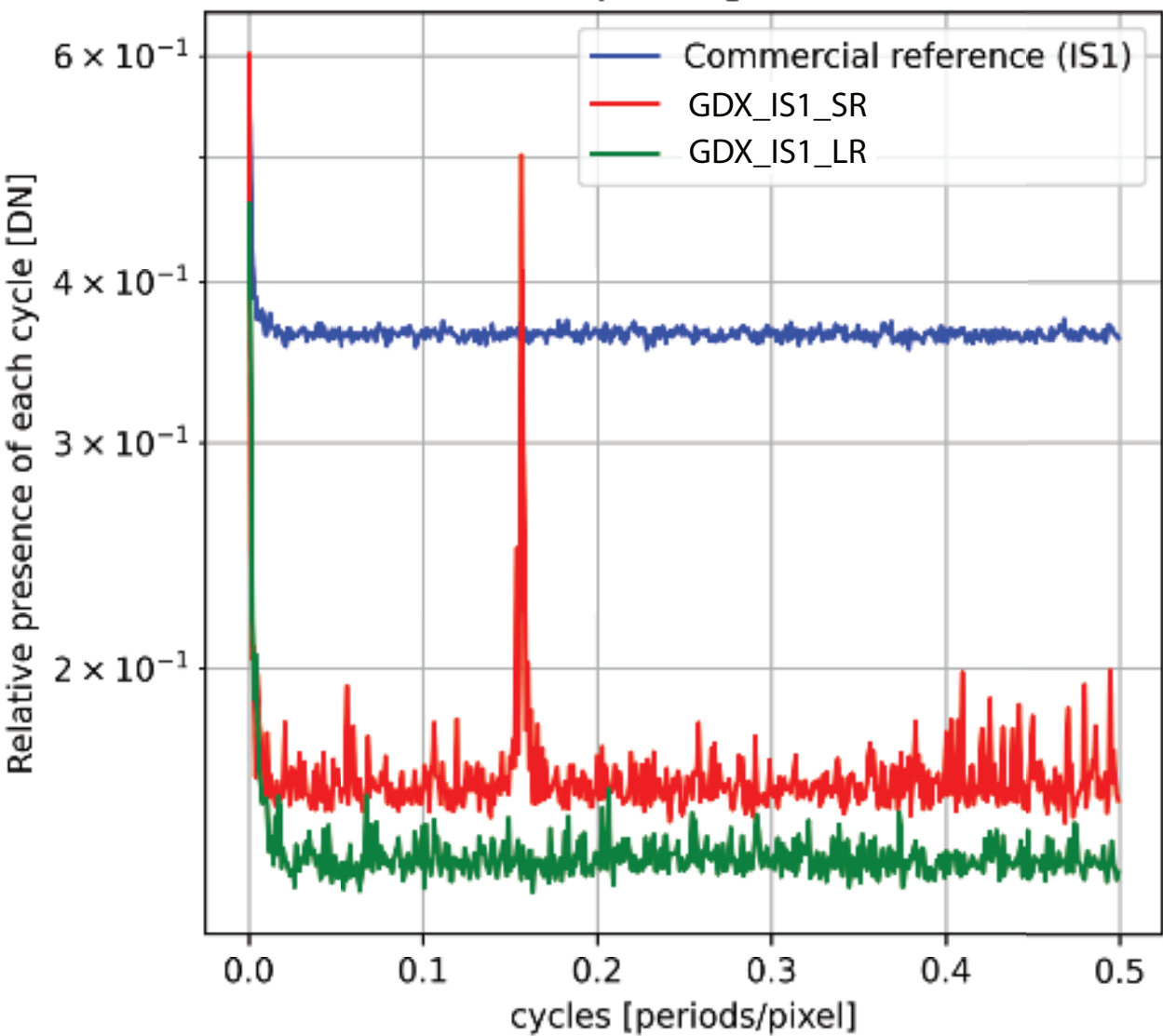
Signal to Noise Ratio

Vertical spectrogram DSNU

Signal to Noise Ratio